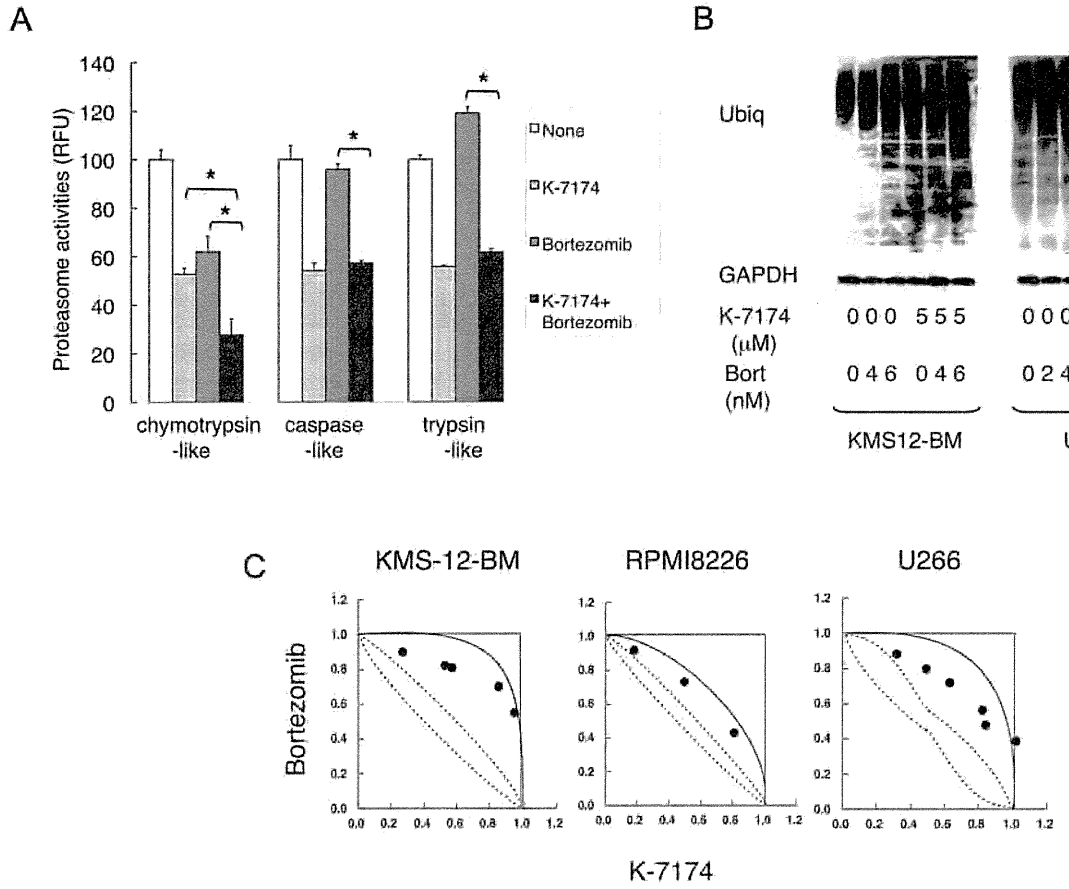

Figure 6. K-7174 and bortezomib exert additive cytotoxicity against MM cell. A. We treated RPMI8226 cells with K-7174 (10 μM), bortezomib (5 nM) or both agents, and determined chymotrypsin-like, caspase-like and trypsin-like activities. Results are represented as relative fluorescence units (RFU) with vehicle controls set at 100%. The means ± S.D. (bars) of three independent experiments are shown. Asterisks indicate $p<0.01$ by paired Student's *t*-test. B. We cultured KMS12-BM, U266 and RPMI8226 cells in the absence or presence of K-7174, bortezomib or both agents for 48 hours at the indicated doses. Whole cell lysates were subjected to immunoblotting for ubiquitinated proteins and GAPDH (internal control). Data are representative of multiple independent experiments. C. Isobolograms of simultaneous exposure of three MM cell lines to K-7174 and bortezomib. The concentrations that produced 80% growth inhibition are expressed as 1.0 on the ordinate and abscissa of isobolograms. The envelope of additivity, surrounded by solid and broken lines, was constructed from dose–response curves of bortezomib and K-7174. The combination is regarded as additive, because all data points fall within the envelope of additivity. The isobolograms shown are representative of at least three independent experiments. Each point represents the mean of at least three independent experiments; standard deviations were less than 25% and were omitted.
doi:10.1371/journal.pone.0060649.g006

hydrophobic interaction, whereas bortezomib binds to the ß5 subunit via a hydrogen-bond network, explaining why higher concentrations are required for HPDs compared with bortezomib. Therefore, the development of novel HPDs with higher activity and specificity is essential for clinical translation. Our finding on the chemical structure of homopiperazine-derived PIs may be of great help in this regard.

Despite the great success of bortezomib in the treatment of refractory malignancies such as MM and mantle cell lymphoma [3,4], we still intend to develop orally bioavailable PIs with distinct mechanisms of action from bortezomib. Several novel PIs, such as carfilzomib [42,43], NPI-0052 [44], CEP-18770 [45], MLN9708 [46], and ONX-0912 [47], are now undergoing clinical trials and show considerable benefits for refractory/relapsed cases as well as untreated MM patients. Among them, carfilzomib and its derivative ONX-0912 are peptide derivatives and have greater selectivity for the ß5 subunit than bortezomib. Although NPI-0052 is a non-peptide PI targeting all three proteasome subunits, its effect was strong for chymotrypsin-like (ß5), moderate for trypsin-like (ß2), and weak for caspase-like (ß1) activities [44]. In addition, NPI-0052 is intravenously administered in clinical studies [48], although it is expected to have oral bioactivity [44]. MLN9708 is orally available and its efficacy has been demonstrated in phase I clinical trials with oral administration [49]; however, this drug is speculated to be ineffective for MM carrying ß5-subunit mutations because of its boronate-based structure similar to bortezomib. Recently, in contrast to our speculation, Chauhan et al. [50] reported the effectiveness of MLN9708 to overcome bortezomib resistance. As several mechanisms have been proposed for bortezomib resistance in addition to ß5 subunit mutations [51], MLN9708 may be effective for such cases.

HPDs are expected to compensate for the weak points of bortezomib as well as the second generation PIs described above, because HPDs are non-peptide agents that inhibit all three catalytic subunits of the proteasome with equal kinetics and could be orally bioactive. Moreover, crystal structure analyses indicate that the binding mode is completely different from that of bortezomib [39] and NPI-0052 [52]. This ensures the activity of this agent against bortezomib-resistant cells, which was experimentally proven in this study, and probably against cells de-

veloping the resistance to NPI-0052. Moreover, we have found that oral administration of K-7174 is indeed effective and is not associated with obvious toxicities, including leukocytopenia, in a murine xenograft model (manuscript in preparation). These features provide a rationale for the clinical translation of HPDs as novel PIs with effectiveness for the treatment of bortezomib-resistant patients, a low probability of acquired drug resistance, and flexibility in dosing schedules.

Acknowledgments

We are grateful to Dr. Hiroaki Kimura (Jichi Medical University) for helpful discussions and technical advice. We are indebted to Ms. Akiko Yonekura for excellent technical assistance.

Author Contributions

Conceived and designed the experiments: JK NS S-YP YF. Performed the experiments: JK NS SY TW MN KS MO S-YP. Analyzed the data: JK NS S-YP YF. Contributed reagents/materials/analysis tools: TI MA YK. Wrote the paper: JK NS S-YP YF.

References

1. Sawyers C (2004) Targeted cancer therapy. Nature 432: 294–297.
2. Weissman AM, Shabek N, Ciechanover A (2011) The predator becomes the prey: regulating the ubiquitin system by ubiquitination and degradation. Nat Rev Mol Cell Biol 12: 605–620.
3. Frankland-Searby S, Bhaumik SR (2012) The 26S proteasome complex: An attractive target for cancer therapy. Biochem Biophys Acta 1825: 64–76.
4. Richardson PG, Mitsiades C, Schlossman R, Ghobrial I, Hideshima T, et al. (2008) Bortezomib in the front-line treatment of multiple myeloma. Expert Rev Anticancer Ther 8: 1053–1072.
5. Kikuchi J, Wada T, Shimizu R, Izumi T, Akutsu M, et al. (2010) Histone deacetylases are critical targets of bortezomib-induced cytotoxicity in multiple myeloma. Blood 116: 406–417.
6. Mannava S, Zhuang D, Nair JR, Bansal R, Wawrzyniak JK, et al. (2012) KLF9 is a novel transcriptional regulator of bortezomib- and LBH589-induced apoptosis in multiple myeloma cells. Blood 119: 1450–1458.
7. Yanamandra N, Colaco NM, Parquet NA, Buzzeo RW, Boulware D, et al. (2006) Tipifarnib and bortezomib are synergistic and overcome cell adhesion-mediated drug resistance in multiple myeloma and acute myeloid leukemia. Clin Cancer Res 12: 591–599.
8. Noborio-Hatano K, Kikuchi J, Takatoku M, Shimizu R, Wada T, et al. (2009) Bortezomib overcomes cell-adhesion-mediated drug resistance through down-regulation of VLA-4 expression in multiple myeloma. Oncogene 28: 231–242.
9. San Miguel JF, Schlag R, Khuageva NK, Dimopoulos MA, Shpilberg O, et al. (2008) Bortezomib plus melphalan and prednisone for initial treatment of multiple myeloma. New Engl J Med 359: 906–917.
10. Palumbo A, Bringhen S, Rossi D, Cavalli M, Larocca A, et al. (2010) Bortezomib-melphalan-prednisone-thalidomide followed by maintenance with bortezomib-thalidomide compared with bortezomib-melphalan-prednisone for initial treatment of multiple myeloma: A randomized controlled trial. J Clin Oncol 28: 5101–5109.
11. Harrison SJ, Quach H, Link E, Seymour JF, Ritchie DS, et al. (2011) A high rate of durable responses with romidepsin, bortezomib, and dexamethasone in relapsed or refractory multiple myeloma. Blood 118: 6274–6283.
12. Lonial S, Waller EK, Richardson PG, Jagannath S, Orlowski RZ, et al. (2005) Risk factors and kinetics of thrombocytopenia associated with bortezomib for relapsed, refractory multiple myeloma. Blood 106: 3777–3784.
13. Richardson PG, Briemberg H, Jagannath S, Wen PY, Barlogie B, et al. (2006) Frequency, characteristics, and reversibility of peripheral neuropathy during treatment of advanced multiple myeloma with bortezomib. J Clin Oncol 24: 3113–3120.
14. Lu S, Yang J, Song X, Gong S, Zhou H, et al. (2008) Point mutation of the proteasome 5 subunit gene is an important mechanism of bortezomib resistance in bortezomib-selected variants of Jurkat T cell lymphoblastic lymphoma/leukemia line. J Pharmacol Exp Ther 326: 423–431.
15. Oerlemans R, Franke NE, Assaraf YG, Assaraf YG, Cloos J, et al. (2008) Molecular basis of bortezomib resistance: proteasome subunit ß5 (PSMB5) gene mutation and over-expression of PSMB5 protein. Blood 112: 2489–2499.
16. Lu S, Yang J, Chen Z, Gong S, Zhou H, et al. (2009) Different mutants of PSMB5 confer varying bortezomib resistance in T lymphoblastic lymphoma/leukemia cells derived from the Jurkat cell line. Exp Hematol 37: 831–837.
17. Ri M, Iida S, Nakashima T, Miyazaki T, Mori F, et al. (2010) Bortezomib-resistant myeloma cell lines: a role for mutated PSMB5 in preventing the accumulation of unfolded proteins and fatal ER stress. Leukemia 24: 1506–1512.
18. Suzuki E, Demo S, Deu E, Keats J, Arastu-Kapur S, et al. (2011) Molecular mechanisms of bortezomib resistant adenocarcinoma cells. PLoS One 6: e27996.
19. Franke NE, Niewerth D, Assaraf YG, van Meerloo J, Vojtekova K, et al. (2012) Impaired bortezomib binding to mutant ß5 subunit of the proteasome is the underlying basis for bortezomib resistance in leukemia cells. Leukemia 26: 757–768.
20. Kitakaze M, Minamino T, Node K, Takashima S, Funaya H, et al. (1999) Adenosine and cardioprotection in the diseased heart. Jpn Circ J 63: 231–243.
21. Umetani M, Nakao H, Doi T, Iwasaki A, Ohtaka M, et al. (2000) A novel cell adhesion inhibitor, K-7174, reduces the endothelial VCAM-1 induction by inflammatory cytokines, acting through the regulation of GATA. Biochem Biophys Res Commun 272: 370–374.
22. Imagawa S, Nakano Y, Obara N, Suzuki N, Doi T, et al. (2003) A GATA-specific inhibitor (K-7174) rescues anemia induced by IL-1ß, TNF-α, or L-NMMA. FASEB J 17: 1742–1744.
23. Nakano Y, Imagawa S, Matsumoto K, Stockmann C, Obara N, et al. (2004) Oral administration of K-11706 inhibits GATA binding activity, enhances hypoxia-inducible factor 1 binding activity, and restores indicators in an in vivo mouse model of anemia of chronic disease. Blood 104: 4300–4307.
24. Takano Y, Hiramatsu N, Okamura M, Hayakawa K, Shimada T, et al. (2007) Suppression of cytokine response by GATA inhibitor K-7174 via unfolded protein response. Biochem Biophys Res Commun 360: 470–475.
25. Drexler HG, Matsuo Y, MacLeod RA (2003) Persistent use of false myeloma cell lines. Hum Cell 16: 101–105.
26. Uno K, Inukai T, Kayagaki N, Goi K, Sato H, et al. (2003) TNF-related apoptosis-inducing ligand (TRAIL) frequently induces apoptosis in Philadelphia chromosome-positive leukemia cells. Blood 101: 3658–3667.
27. de Leeuw RJ, Davies JJ, Rosenwald A, Bebb G, Gascoyne RD, et al. (2004) Comprehensive whole genome array CGH profiling of mantle cell lymphoma model genomes. Hum Mol Genet 13: 1827–1837.
28. Mitsunaga K, Kikuchi J, Wada T, Furukawa Y (2012) Latexin Regulates the abundance of multiple cellular proteins in hematopoietic stem cells. J Cell Physiol 227: 1138–1147.
29. Meng L, Mohan R, Kwok BH, Elofsson M, Sin N, et al. (1999) Epoxomicin, a potent and selective proteasome inhibitor, exhibits in vivo antiinflammatory activity. Proc Natl Acad Sci USA 96: 10403–10408.
30. Smith DM, Wang Z, Kazi A, Li LH, Chan,TH, et al. (2002) Synthetic analogs of green tea polyphenols as proteasome inhibitors. Mol Med 8: 382–392.
31. Otwinowski Z, Minor W (1997) Processing of X-ray diffraction data collection in oscillation mode. Method Enzymol 276: 307–326.
32. Vagin A, Teplyakov A (2000) An approach to multi-copy search in molecular replacement. Acta Crystallogr D Biol Crystallogr 56: 1622–1624.
33. Adams PD, Grosse-Kunstleve RW, Hung LW, Ioerger TR, McCoy AJ, et al. (2002) PHENIX: building new software for automated crystallographic structure determination. Acta Crystallogr D Biol Crystallogr 58: 1948–1954.
34. Emsley P, Cowtan K (2004) Coot: model-building tools for molecular graphics. Acta Crystallogr D Biol Crystallogr 60: 2126–2132.
35. Davis IW, Murray LW, Richardson JS, Richardson DC (2004) MOLPROBITY: structure validation and all-atom contact analysis for nucleic acids and their complexes. Nucleic Acids Res 32: W615–619, doi:10.1093/nar/gkh398.
36. Kikuchi J, Shimizu R, Wada T, Ando H, Nakamura M, et al. (2007) E2F-6 suppresses growth-associated apoptosis of human hematopoietic progenitor cells by counteracting proapoptotic activity of E2F-1. Stem Cells 25: 2439–2447.
37. Wada T, Kikuchi J, Furukawa Y (2012) Histone deacetylase 1 enhances microRNA processing via deacetylation of DGCR8. EMBO Rep 13: 142–149.
38. Furukawa Y, Vu HA, Akutsu M, Odgerel T, Izumi T, et al. (2007) Divergent cytotoxic effects of PKC412 in combination with conventional antileukemic agents in FLT3 mutation-positive versus-negative leukemia cell lines. Leukemia 21: 1005–1014.
39. Groll M, Berkers CR, Ploegh HL, Ovaa H (2006) Crystal structure of the boronic acid-based proteasome inhibitor bortezomib in complex with the yeast 20 S proteasome. Structure 14: 451–456.
40. De Bettignies G, Coux O (2010) Proteasome inhibitors: Dozens of molecules and still counting. Biochimie 92: 1530–1545.
41. Ruschak AM, Slassi M, Kay LE, Schimmer AD (2011) Novel proteasome inhibitors to overcome bortezomib resistance. J Natl Cancer Inst 103: 1007–1017.
42. Kuhn DJ, Chen Q, Voorhees PM, Strader JS, Shenk KD, et al. (2007) Potent activity of carfilzomib, a novel, irreversible inhibitor of the ubiquitin-proteasome pathway, against preclinical models of multiple myeloma. Blood 110: 3281–3290.
43. O'Connor OA, Stewart AK, Vallone M, Molineaux CJ, Kunkel LA, et al. (2009) A phase I dose escalation study of the safety and pharmacokinetics of the novel proteasome inhibitor carfilzomib (PR-171) in patients with hematological malignancies. Clin Cancer Res 15: 7085–7091.
44. Chauhan D, Catley L, Li G, Podar K, Hideshima T, et al. (2005) A novel orally active proteasome inhibitor induces apoptosis in multiple myeloma cells with mechanisms distinct from Bortezomib. Cancer Cell 8: 407–419.

45. Piva R, Ruggeri B, Williams M, Costa G, Tamagno I, et al. (2008) CEP-18770: A novel, orally active proteasome inhibitor with a tumor-selective pharmacologic profile competitive with bortezomib. Blood 111: 2765–2775.
46. Kupperman E, Lee EC, Cao Y, Bannerman B, Fitzgerald M, et al. (2010) Evaluation of the proteasome inhibitor MLN9708 in preclinical models of human cancer. Cancer Res 70: 1970–1980.
47. Chauhan D, Singh AV, Aujay M, Kirk CJ, Bandi M, et al. (2010) A novel orally active proteasome inhibitor ONX 0912 triggers in vitro and in vivo cytotoxicity in multiple myeloma. Blood 116: 4906–4915.
48. Millward M, Price T, Townsend A, Sweeney C, Spencer A, et al. (2012) Phase 1 clinical trial of the novel proteasome inhibitor marizomib with the histone deacetylase inhibitor vorinostat in patients with melanoma, pancreatic and lung cancer based on in vitro assessments of the combination. Invest New Drugs 30: 2303–2317.
49. Moreau P, Richardson PG, Cavo M, Orlowski RZ, San Miguel JF, et al. (2012) Proteasome inhibitors in multiple myeloma: 10 years later. Blood 120: 947–959.
50. Chauhan D, Tian Z, Zhou B, Kuhn D, Orlowski R, et al. (2011) In vitro and in vivo selective antitumor activity of a novel orally bioavailable proteasome inhibitor MLN9708 against multiple myeloma cells. Clin Cancer Res 17: 5311–5321.
51. Mujtaba T, Dou QP (2011) Advances in the understanding of mechanisms and therapeutic use of bortezomib. Discov Med 12: 471–480.
52. Groll M, Huber R, Potts BC (2006) Crystal structures of salinosporamide A (NPI-0052) and B (NPI-0047) in complex with the 20 S proteasome reveal important consequences of β-lactone ring opening and a mechanism for irreversible binding. J Am Chem Soc 128: 5136–5141.

Journal of Bioscience and Bioengineering
VOL. 115 No. 5, 497–506, 2013

ELSEVIER

www.elsevier.com/locate/jbiosc

Roles of conserved Arg^{72} and Tyr^{71} in the ascorbate-specific transmembrane electron transfer catalyzed by *Zea mays* cytochrome b_{561}

Motiur Md. Rahman,[1] Nobuyuki Nakanishi,[1] Yoichi Sakamoto,[2] Hiroshi Hori,[2,3] Toshiharu Hase,[4] Sam-Yong Park,[5] and Motonari Tsubaki[2,*]

Department of Molecular Science and Material Engineering, Graduate School of Science and Technology, Kobe University, 1-1 Rokkodai-cho, Nada-ku, Kobe, Hyogo 657-8501, Japan,[1] Department of Chemistry, Graduate School of Science, Kobe University, 1-1 Rokkodai-cho, Nada-ku, Kobe, Hyogo 657-8501, Japan,[2] Center for Quantum Science and Technology under Extreme Conditions, Osaka University, 1-3 Machikaneyama-cho, Toyonaka, Osaka 560-8531, Japan,[3] Institute for Protein Research, Osaka University, Suita, Osaka 565-0871, Japan,[4] and Division of Science of Biological Supramolecular Systems, Graduate School of Integrated Science, Yokohama City University, Yokohama, Kanagawa 230-0045, Japan[5]

Received 16 September 2012; accepted 19 November 2012
Available online 3 January 2013

Cytochromes b_{561}, novel transmembrane electron transport proteins residing in eukaryotic cells, have a number of common features including six transmembrane α-helices and two heme ligation sites. Our recent studies on recombinant *Zea mays* cytochrome b_{561} suggested that concerted proton/electron transfer mechanism was functioning in plant cytochromes b_{561} as well and that conserved Lys^{83} on a cytosolic loop had important roles for ascorbate-binding and a succeeding electron transfer. In the present study, we conducted site-directed mutagenesis analyses on conserved Arg^{72} and Tyr^{71}. Removal of a positive charge at Arg^{72} did not affect significantly on the final heme reduction level with ascorbate as reductant. However, characteristic pH-dependent initial time-lag upon electron acceptance from ascorbate was completely lost for R72A and R72E mutants. Substitution of Tyr^{71} with Ala or Phe affected both on the final heme reduction level and on the pH-dependent initial time-lag, causing acceleration of the electron transfer. These observations were interpreted as existence of specific interactions of Tyr^{71} and Arg^{72} with ascorbate. However, their mechanistic roles were distinctly different from that of Lys^{83}, as exemplified by K83A/Y71A double mutant, and might be related for expelling of monodehydroascorbate radical from the substrate-binding site to prevent a back-flow of electrons.

[**Key words:** Cytochrome b_{561}; Ascorbate; Monodehydroascorbate radical; Transmembrane electron transfer; Membrane protein]

During the past several decades, evidence has accumulated on the presence of specific high-potential ascorbate-reducible *b*-type cytochrome in the plasma membranes of higher plants (1–4). The cytochrome is named as cytochrome b_{561} based on the similarities, such as α-band peak at 561 nm, reducibility with ascorbate, and positive midpoint potentials (+110–160 mV), to the *b*-type cytochrome present in chromaffin granules (CG) of animal cells (5–7). Of particular interest are recent discoveries of a number of plant genes that encode transmembrane proteins having striking homology to mammalian adrenal CG cytochrome b_{561} (8). These cytochromes b_{561} residing in large variety of eukaryotic cells, including Dcytb identified in the duodenal plasma membrane (9), Lcytb (10), and 101F6 (11,12), were found to constitute a novel class of transmembrane electron transport proteins (13).

A number of highly relevant structural features, including six hydrophobic transmembrane α-helices, two heme ligation sites, and possible ascorbate (AsA) and monodehydroascorbate (MDA) radical binding sequences (7,14–16), are almost perfectly conserved among the members of animal and plant cytochrome b_{561} subfamilies. It was postulated that two heme *b* prosthetic groups are located near the putative AsA-binding sequence on the cytosolic side and the putative MDA radical-binding sequence on the intravesicular side to perform a unique transmembrane electron transfer (13,14). In the case of bovine adrenal CG cytochrome b_{561}, this postulation was verified using various biochemical and biophysical techniques (15–17). Particularly, our pulse radiolysis experiment on the purified sample in a detergent-solubilized state showed conclusively that the high-potential heme on the intravesicular side has a role for the fast electron donation to MDA radical whereas the low-potential heme on the cytosolic side is responsible for the electron acceptance from AsA (18). Further, our stopped-flow analysis on the diethylpyrocarbonate (DEPC)-modified cytochrome b_{561} confirmed that the low-potential heme on the cytosolic side is the site for the entrance of electrons from AsA, even though both hemes can be theoretically accessible by AsA in the

* Corresponding author. Tel./fax: +81 78 803 6582.
E-mail address: mtsubaki@kobe-u.ac.jp (M. Tsubaki).

Abbreviations: AsA, ascorbate; CG, chromaffin granule; DEPC, diethylpyrocarbonate; EPR, electron paramagnetic resonance; MALDI-TOF, matrix assisted laser desorption/ionization-time of flight; MDA, monodehydroascorbate; β-OG, *n*-octyl-β-D-glucoside; Zmb$_{561}$, *Zea mays* cytochrome b_{561}.

1389-1723/$ – see front matter © 2012, The Society for Biotechnology, Japan. All rights reserved.
http://dx.doi.org/10.1016/j.jbiosc.2012.11.013

detergent-solubilized state (17). Thus, clarification of the molecular mechanism for such site-specificity is our current interest.

For plant cytochromes b_{561}, however, there have been only a few detailed studies being conducted. This is primarily due to the difficulty in the purification from plant tissues (1,2,19). However, recent progress in the studies on plant cytochromes b_{561} suggested that they utilize AsA as a physiological electron donating substrate (20–22) to supply electron equivalents *via* transmembrane electron transfer to other reactions operative on the opposite side of the membranes. For the physiological functions of the plant cytochrome b_{561}, two possibilities might be raised. As one possible role, it might utilize AsA as the physiological substrate on the cytosolic side to regenerate AsA on the other side of membranes, as found for adrenal CG cytochrome b_{561} (23). Such regenerated AsA on the other side of membranes might be used for cell growth and cell division and/or coupling to other redox proteins (3,21). The other possibility is that plant cytochrome b_{561} might work as a transmembrane ferrireductase to reduce ferric ion to ferrous state (22) and have an indirect role for the cellular iron absorption (or storage), as proposed for Dcytb (9). Indeed, it was shown that a member of cytochrome b_{561} family had a ferrireductase activity more or less (24,25). However, since the sub-cellular and tissue-specific localization of plant cytochromes b_{561} was still not completely understood (20,21,26,27), it might be too early to make conclusive arguments. For the better understanding of exact physiological role(s) of these unique plant membrane proteins, detailed studies concerning the molecular mechanism of transmembrane electron transfer reaction might be required.

Recently, we have succeeded in the construction of a heterologous expression system for *Zea mays* cytochrome b_{561} (Zmb_{561}) (Fig. 1) using methylotrophic yeast *Pichia pastoris* cells, established its purification procedure, and opened a new way for detailed biochemical and biophysical analyses (28,29). Our analysis using stopped-flow and pulse radiolysis techniques indicated that purified wild-type *Z. mays* cytochrome b_{561} (WT-Zmb_{561}) protein had significant activities for the electron donation to MDA radical and the electron acceptance from AsA (29). Further, our comparative study on WT-Zmb_{561} with bovine adrenal CG cytochrome b_{561} using a site-specific chemical modification technique demonstrated that the concerted proton/electron transfer mechanism, which was hypothesized to be operative in bovine adrenal CG cytochrome b_{561} upon electron acceptance from AsA (30), was clearly working in Zmb_{561} as well (31). We also performed a site-directed mutagenesis study on Zmb_{561} with particular interests on the conserved amino acid residues residing in the putative AsA and MDA radical binding sequences (29). Among the mutants examined, three site-directed mutants, K83A, K83E, and K83D, showed a significant decrease in their electron accepting ability from AsA, indicating that the well-conserved Lys^{83} has a very important role for the binding of and the electron transfer from AsA (29).

In the present study, we focused on two amino acid residues (Tyr^{71} and Arg^{72}) residing in the same loop with that of Lys^{83} as

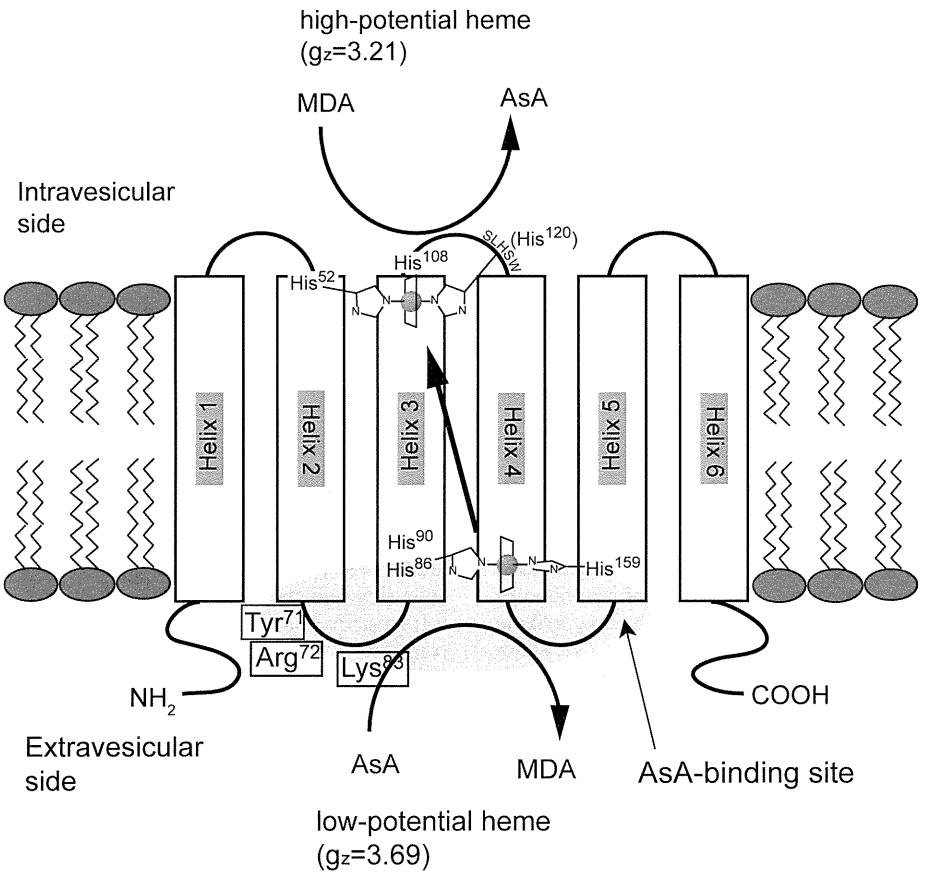

FIG. 1. The six transmembrane helices model of *Zea mays* cytochrome b_{561}. *Zea mays* cytochrome b_{561} (Zmb_{561}) is considered to have six transmembrane helices and two hemes *b* centers. Two hemes are located on the intravesicular and extravesicular side, respectively, with different electron paramagnetic resonance (EPR) characters as indicated based on Nakanishi et al. (31). Two well-conserved sequences (ALLVYRVFR, SLHSW) found initially in animal species were predicted as a part of the AsA- and MDA radical-binding site, respectively (14). The latter is also well conserved in plant species and is indicated in a loop connecting helix 3 and 5. On the other hand, the former sequence residing in a loop connecting helix 2 and 3 is partially conserved in plant species. However, both Tyr^{71} and Arg^{72} are well conserved and are expected to have important roles for the electron acceptance from AsA together with well conserved Lys^{83} (29).

targets for the detailed site-directed mutagenesis study (Fig. 1). Both Tyr^{71} (corresponding to Tyr^{73} of bovine adrenal CG cytochrome b_{561}) and Arg^{72} are located within a part of motif1 (13) and putative AsA-binding sequence (14) (Fig. 1). Since the conservation of Tyr^{71} is very high and is one of a few aromatic residues close to the cytosolic heme center, it may have very important roles for the electron accepting reaction from AsA. Thus, we constructed two site-directed mutants, Y71A-H_6 and Y71F-H_6. The second target, Arg^{72}, probably has more important roles in the putative AsA-binding sequence (14). The positive charge of this side-chain group might be participating in a direct interaction with a negatively-charged AsA molecule, in collaboration with other positively-charged residues including Lys^{83} (29), which might have a guiding role for the approach of AsA to the substrate-binding site on the cytosolic side (Fig. 1). Further, AsA-dependent reduction level assay on the site-directed mutants R72A of recombinant mouse adrenal CG cytochrome b_{561} in the yeast membrane fraction (32) and of recombinant bovine adrenal CG cytochrome b_{561} in a purified state (33) indicated the importance of a positive charge for the high-affinity AsA-binding. However, for the recombinant *Arabidopsis thaliana* cytochrome b_{561}, its K70A mutant (the corresponding position to Arg^{72} of Zmb_{561} was replaced with Lys in the *Arabidopsis* cytochrome b_{561}) in yeast microsomal membranes did not show any such effects (34). To solve the apparently contradictory results, we constructed four site-directed mutants, namely, R72A-H_6, R72D-H_6, R72E-H_6 and R72K-H_6. We performed detailed biochemical and biophysical analyses on each of the site-directed mutants in a highly purified state to investigate the physiological and mechanistic roles of these two conserved residues on the cytosolic side for the transmembrane electron transfer reaction.

MATERIALS AND METHODS

Site-directed mutagenesis The cloned full-length Zmb_{561} (AB182641; DDBJ/EMBL/GenBank) was ligated into *EcoR* I-*Xba* I site of pPICZB vector, as described previously (29). We further introduced a hexa-histidine (6x His) sequence at the 3′ end of the Zmb_{561} gene (29). The resulting expression vector, pPICZB-WT-Zmb_{561}-H_6, could express recombinant Zmb_{561} protein with a C-terminal 6x His sequence (WT-Zmb_{561}-H_6). The amino acid sequence of its C-terminal part was, therefore, ^{211}GASVVVAAIAPVRLEEPQGYDPIPENHHHHHH^{242}. Site-specific mutations were, then, introduced using Quikchange II site-directed mutagenesis kit (Stratagene Corp., La Jolla, CA, USA). All the primers, which were used for the mutagenesis, are listed in Table S1. Expression vectors for six site-specific mutants with a C-terminal 6x His-tag moiety (R72A-H_6, R72D-H_6, R72E-H_6, R72K-H_6, Y71A-H_6, and Y71F-H_6) were, thus, constructed. Construction of the expression vector for K83A/Y71A was conducted by introducing a second site-specific mutation on the expression vector for K83A mutant (29) using Quikchange II site-directed mutagenesis kit. These constructs were each confirmed by DNA sequencing using an ABI 3100 Genetic Analyzer (Applied Biosystems, Foster City, CA, USA).

Expression of Zmb_{561} mutants in *P. pastoris*, cells The expression and purification of Zmb_{561} mutants were followed by the procedure as described in our previous studies (28,29).

Purification of Zmb_{561} mutants The expressed WT-Zmb_{561}-H_6 and its site-specific mutants were purified as previously described (28,29,31). Purification of K83A/Y71A was conducted as previously described (29). SDS-PAGE analysis was performed using 15% gels according to the method of Laemmli (35). The concentration of the purified Zmb_{561} samples was each determined spectrophotometrically using a difference extinction coefficient of 27.7 mM^{-1} cm^{-1} at 561 nm *minus* 575 nm in the reduced state (7).

Matrix assisted laser desorption/ionization-time of flight (MALDI-TOF)-mass spectrometry Mass spectrometric analyses were conducted with a Voyager DE Pro mass spectrometer (Applied Biosystems, Foster City, CA, USA) using a 20-kV accelerating voltage. Other experimental conditions were essentially the same as in previously described (15,16,29). All of the recombinant wild-type protein (WT-Zmb_{561}-H_6) and its site-specific mutants (Y71A-H_6, Y71F–H_6, R72A-H_6, R72D-H_6, R72E-H_6, R72K-H_6, and K83A/Y71A) (~100 μM) were each digested either with TPCK-treated trypsin (0.01 mg/mL) or *Staphylococcus aureus* V8 protease (0.01 mg/mL), respectively. After 48 h of incubation at room temperature, the peptide solutions were diluted 1:9 (v/v) with a matrix solution (α-cyano-4-hydroxycinamic acid (Aldrich, Gillingham, England), 50 mg/mL in 50% acetonitrile in 0.3% TFA). The mixtures (typically, 1.0 μL) were deposited on a sample plate, allowed to air-dry, and analyzed. The search of the corresponding fragments in the amino acid sequence of Zmb_{561} mutants was conducted using the program GPMAW (v 6.11) (Lighthouse Data, Odense M, Denmark).

Electron paramagnetic resonance (EPR) spectroscopy Purified Y71A and WT-Zmb_{561} samples (200–300 μM) in 50 mM potassium phosphate (pH 7.0) buffer containing 1.0 % (w/v) *n*-octyl-β-D-glucoside (β-OG) were introduced into EPR tubes and were frozen in liquid nitrogen (77 K) immediately. EPR measurements were carried out at X-band (9.23 GHz) microwave frequency using a Varian E-12 EPR spectrometer with 100-kHz field modulation, as previously described (7,29).

AsA-reduction level assay Eight purified Zmb_{561} mutants (Y71A-H_6, Y71F-H_6, R72A-H_6, R72D-H_6, R72E-H_6, R72K-H_6, K83A, and K83A/Y71A) and wild-type protein (WT-Zmb_{561}-H_6) were each diluted to 1 μM with 50 mM potassium-phosphate buffer (pH 7.0, 6.0) or 50 mM sodium acetate buffer (pH 5.0) each containing 1.0 % (w/v) β-OG. After 30 min of incubation at room temperature, UV–visible absorption spectra of the mutants in oxidized and dithionite-reduced states were measured from 700 to 200 nm with a UV-2400PC spectrophotometer (Shimadzu Corp., Kyoto, Japan). For the AsA-reduced state of the mutants, the absorbance change at 425 nm was recorded for 30 min after the addition of AsA (10 mM) although the equilibrium was attained within 30 s after the addition. Then, the spectra were measured. The final reduction level with AsA as a reductant was calculated based on the dithionite-reduced form as the 100% reduction level.

Redox titrations Spectroscopic titrations were performed as described by Dutton (36) and Takeuchi (16), using a Shimadzu UV-2400PC spectrometer equipped with a thermostated cell holder connected to a low temperature thermobath (NCB-1200, Tokyo Rikakikai Co, Ltd, Tokyo, Japan). During the measurements, visible absorption spectra and redox potentials were recorded in an appropriate interval, as previously described (29). The changes in absorbance ($A_{561.0}$ *minus* $A_{566.8}$, the latter corresponding to the isosbestic point of WT-Zmb_{561}-H_6) were corrected with the dilution effect and analyzed with Igor Pro (v. 6.03A2) employing a Nernst equation with two redox components; i.e., with a linear combination of two sigmoid functions;

$$f(x) = \text{base} + (\text{max} * 1/(1 + \exp((x1 - x)/\text{slope } 1))) + (\text{max} * 1/(1 + \exp((x2 - x)/\text{slope } 2))) \quad (1)$$

in which base, max, slope 1, and slope 2 were fixed as 100, −50, 25.62, and 25.62, respectively, during the curve-fitting procedure, and ×1 and ×2 gave the estimated midpoint potentials (in mV), respectively. Potentials are expressed relative to the normal hydrogen electrode (NHE).

Stopped-flow analyses Rapid kinetic measurements were carried out using an RSP-1000-03DR stopped-flow spectrometer (Unisoku, Osaka, Japan). Purified WT-Zmb_{561}-H_6 or either of its site-directed mutants (Y71A-H_6, Y71F-H_6, R72A-H_6, R72D-H_6, R72E-H_6, R72K-H_6, K83A, and K83A/Y71A) in oxidized state was each diluted to 2 μM with 50 mM potassium-phosphate buffer (pH 7.0, 6.0) or 50 mM sodium acetate buffer (pH 5.0) each containing 1.0% (w/v) β-OG. After 30 min of incubation at room temperature, protein solution and AsA solution were loaded into a different chamber of the apparatus, respectively. The temperature of both chambers was maintained at 20°C by connecting to a thermobath. Mixing of the two solutions was carried out with a 1:1 volume ratio and the heme absorbance change at 427 nm due to the reduction with AsA was recorded against time. Data points were collected in every 250 μs for the measurements of time duration of 1 s and in every 2.5 ms and 15 ms for the measurements of time duration of 10 s and 60 s, respectively. Both Igor Pro software (v. 6.03) and a built-in software of the stopped-flow apparatus were used for data analyses. For the measurements of K83A and K83A/Y71A, the samples without 6x His-tag moiety were used. We found previously that presence of 6x His-tag moiety of WT-Zmb_{561} did not cause any significant influences on the electron transfer from AsA (29,31). Other experimental conditions were described previously (29,31).

RESULTS

MALDI-TOF-mass spectrometric analyses and visible absorption spectra of purified *Z. mays* cytochrome b_{561} and its site-specific mutants Purified recombinant wild-type proteins (WT-Zmb_{561}-H_6 and WT-Zmb_{561}) and their site-directed mutants (Y71A-H_6, Y71F-H_6, R72A-H_6, R72D-H_6, R72E-H_6, R72K-H_6, K83A, and K83A/Y71A) were each examined by MALDI-TOF-mass spectrometry to verify the site-specific mutations (Tables S2–S7, Figs. S1–S7). All the purified samples showed characteristics visible absorption spectra as a member of the cytochrome b_{561} family, with peaks at 414 nm for the oxidized form and at 561, 529, and 427 nm for the dithionite-reduced form. As a representative example, UV–visible spectra of R72A-H_6 mutant in oxidized, AsA-reduced, and dithionite-reduced states are shown in Fig. 2A, indicating close similarities to those of WT-Zmb_{561} (29) and of bovine adrenal CG cytochrome b_{561} (7) (for other mutants, spectra not

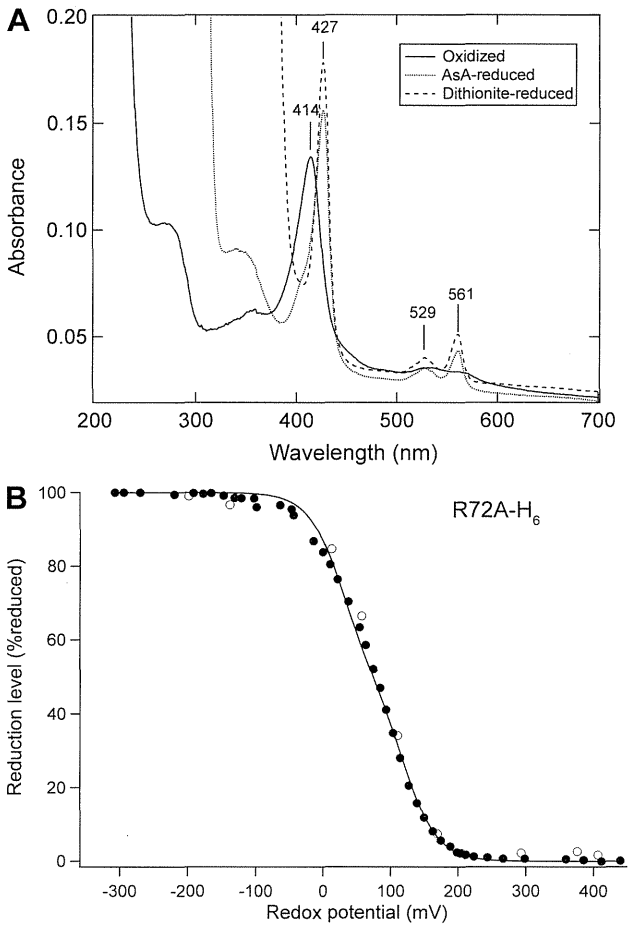

FIG. 2. Absorption spectra of oxidized, AsA-reduced and dithionite-reduced forms of R72A-H_6 (A) and potentiometric behaviors of R72A-H_6 by the least-square curve-fitting analysis (B). (A) After 30 min of incubation of R72A-H_6 with AsA (10 mM) in 20 mM Na-phosphate buffer (pH 7.0), 1.0% (w/v) β-OG, its UV–visible absorption spectrum was recorded and was compared with those in oxidized and in dithionite-reduced states. (B) Percentages of the reduction level of R72A-H_6 *vs.* redox potential were calculated based on the absorbance difference of α-band peak (561.0 nm) and an isosbestic point (567.2 nm). Solid and open circles indicate data points for the reductive and the oxidative titrations, respectively. A least-square curve-fitting on the data points of the reductive phase was conducted by assuming two distinct redox components; i.e., with a linear combination of two sigmoid functions. Other details are described in the text.

shown). These results suggested that all the mutations introduced did not affect significantly on the overall structure of the Zmb_{561} molecule or even the local structure around the immediate surroundings of two heme *b* prosthetic groups.

EPR spectroscopy EPR spectrum measured at 5 K of oxidized Y71A, which was chosen as a representative example for evaluation of the mutation in the cytosolic loop, showed a g_z-signal from a low-spin heme with the HALS (highly anisotropic low-spin) character (37) and a g_z-signal from the other heme with the rhombic character. The former EPR signal, assigned to the cytosolic heme center (7), was actually composed of two signals with slightly different g_z values (g_z = 3.70 and 3.59) (Fig. S8), in which the latter signal (g_z = 3.59) was not observed in those of oxidized WT-Zmb_{561} and K83A measured at 5 K (29). On the other hand, the other low-spin heme signal (g_z = 3.15) assignable to the intravesicular heme center (7) lost its relative intensity slightly compared to those of WT-Zmb_{561} and K83A mutant (29). When measured at 15 K, a new low-spin EPR species with g_z = 2.90 and g_y = 2.27 signals dominated in the spectrum (Fig. S8).

The pH-dependent behavior of the final reduction level To evaluate overall influences of the mutations introduced, we investigated the final heme reduction level with AsA (10 mM) as a reductant at three different pH (Fig. 3A and B). At pH 7.0, addition of AsA (10 mM) to the oxidized WT-Zmb_{561}-H_6 caused a quick reduction of heme *b* reaching the final reduction level of ~80%, as previously reported (29,31), being consistent with the notion that Zmb_{561} utilize AsA as a physiological reductant in *Z. mays* cells. Four site-specific mutants (R72A-H_6, R72D-H_6, R72E-H_6, and R72K-H_6) for Arg^{72}, which is located on the cytosolic side of the molecule, did not show any significant changes in the final heme reduction level nor any significant pH-dependency (Fig. 3A). On

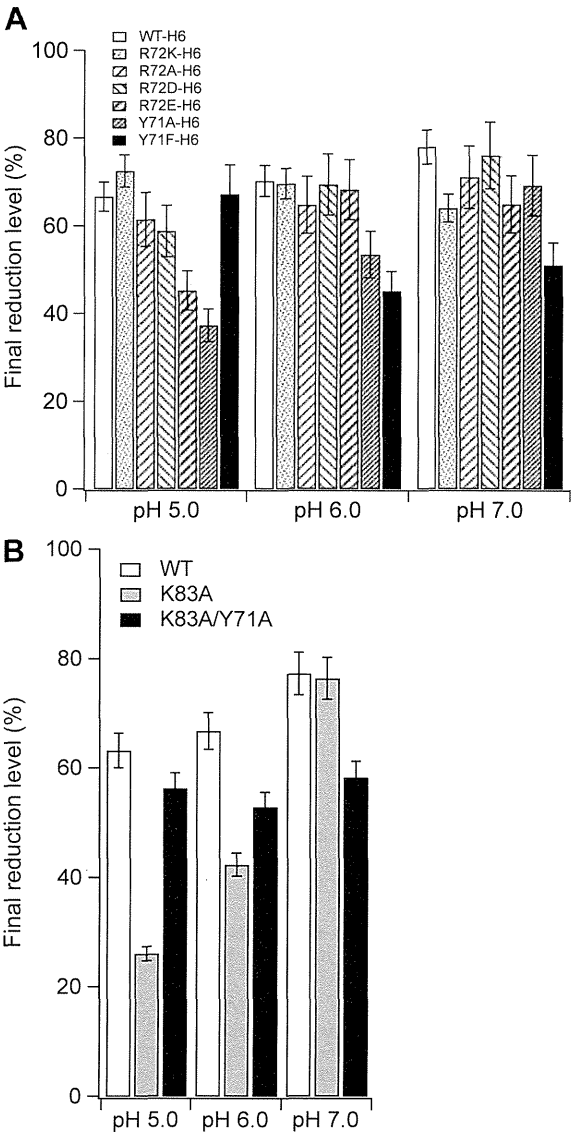

FIG. 3. Effects of pH change on the final heme reduction levels of WT-Zmb_{561}-H_6 and WT-Zmb_{561} and their mutants using AsA as a reductant. (A) After 30 min of incubation of WT-Zmb_{561}-H_6, R72A-H_6, R72D-H_6, R72E-H_6, Y71A-H_6, and Y71F-H_6 with AsA (10 mM) in buffer containing 1.0% (w/v) β-OG with three different pH (5.0, 6.0, and 7.0) at room temperature, their respective UV–visible absorption spectrum was recorded and was compared with those in oxidized and in the dithionite-reduced states. The final heme reduction levels with AsA as a reductant were calculated from the spectra based on the dithionite-reduced form as the 100 % level. (B) After 30 min of incubation of WT-Zmb_{561}, K83A, and K83A/Y71A with AsA (10 mM) in buffer containing 1.0 % (w/v) β-OG with three different pH (pHs 5.0, 6.0, and 7.0) at room temperature, their respective UV–visible absorption spectrum was recorded and was compared with those in oxidized and in the dithionite-reduced states.

the other hand, Y71A-H_6 mutant showed a much lower heme reduction level than those of WT-Zmb_{561}-H_6 with AsA at pH 5.0, indicating slight pH-dependent changes (Fig. 3A). Y71F–H_6 mutant showed a very different property from those of WT-Zmb_{561}-H_6 and other mutants. It showed a very high reduction level at pH 5.0, whereas, at pH 6.0 and 7.0, the reduction level became lowered than the others (45–50%) (Fig. 3A).

Very interestingly, upon analysis of K83A/Y71A double mutant, we found that the significant lowering of heme reduction level caused by the K83A mutation at pH 5.0 (29) was apparently rescued by introducing a second mutation of Y71A (Fig. 3B).

Effects of mutations on the redox potentials of Zmb_{561} As previously reported (29), the apparent midpoint potential of WT-Zmb_{561}-H_6 was estimated as +66 mV and midpoint potentials of the higher and the lower redox components showed +119 and +11 mV, respectively, after the curve-fitting analysis with a least-square method assuming two distinct redox components (Table 1). We confirmed further that there was no distinct effect upon removal of the 6x His-tag moiety (for WT-Zmb_{561}; apparent midpoint potential, +64 mV; higher and lower redox components as +118 and +9 mV, respectively) (Table 1). Mutations of Arg^{72} did not affect significantly on the redox potentials of both heme centers (Table 1). A typical example (for R72A-H_6) is shown (Fig. 2B). On the other hand, mutations of Tyr^{71} did affect significantly on both heme centers; the center with a higher redox potential showed a decrease by 30–40 mV, whereas the center with a lower redox potential showed a significant decrease by ~10 mV for Y71A-H_6 and ~80 mV for Y71F-H_6 (Table 1). Results of the analyses for Y71A-H_6 and Y71F-H_6 are shown in (Figs. S9 and S10), respectively. The K83A/Y71A mutant showed similar redox potentials with those of Y71A-H_6 (Table 1) rather than those of K83A (29).

Stopped-flow analyses of WT-Zmb_{561}-H_6 and its site-specific mutants The electron accepting reaction of oxidized WT-Zmb_{561}-H_6 and its site-directed mutants were analyzed by stopped-flow spectrometry (Fig. 4A). As a representative example, the absorbance change at 427 nm after mixing of oxidized WT-Zmb_{561}-H_6 (final, 1 μM) with AsA (final, 2 mM) was presented against time in a logarithmic scale (Fig. 4Aa). The result showed that, in the initial phase of the electron acceptance from AsA, the heme reduction rate of WT-Zmb_{561}-H_6 was much slower at pH 5.0 than that measured at pH 7.0, as observed for bovine adrenal CG cytochrome b_{561} (17) and for WT-Zmb_{561} (29). On the other hand, such an initial time-lag at pH 5.0 was almost completely absent for R72A-H_6 (Fig. 4Ab) and R72E-H_6 (Fig. 4Ad) mutants. For R72D-H_6 mutant, the initial time-lag at pH 5.0 still persisted but with a much reduced extent (Fig. 4Ac). It might be stressed that there were not so much pH-dependency in the initial apparent rate constants for the R72A-H_6 and R72E-H_6 mutants and these values were very similar to those of WT-Zmb_{561}-H_6 measured at pH 6.0 (Fig. 4Aa).

Time-courses of the reduction process with AsA for both Y71A-H_6 and Y71F-H_6 mutants were also analyzed by stopped-flow spectrometry. In the case of Y71A-H_6, the initial time-lag at pH 5.0 was almost absent (Fig. 4Ae). Further, overall reduction process of Y71A-H_6 with AsA was similar to (or even faster than) those of R72A-H_6 (Fig. 4Ab) and R72E-H_6 (Fig. 4Ac) mutants. Surprisingly, acceleration of the electron transfer from AsA to the heme at pH 5.0 was clearly seen for Y71F-H_6 mutant (Fig. 4Af) when compared with the time-courses of WT-Zmb_{561}-H_6 and the R72 mutants.

For clarification of these analyses, we also calculated the apparent rate constants (k_{app} (sec^{-1})) of the reduction processes corresponding to the plotted data in Fig. 4A and the results are tabulated in Table S8. For the calculation, we assumed a single exponential decay for the initial 10 s and 60 s after the mixing with AsA for the simplicity. This treatment was based on the notion that the entire reduction of Zmb_{561} is actually composed of two succeeding steps; i.e., an initial fast electron accepting reaction from AsA at the cytosolic heme and a following slow long-range electron transfer from the reduced cytosolic heme to the oxidized intravesicular heme (17,18). It is obvious from Table S8 that, at pH 5.0, WT-Zmb_{561}-H_6 and R72D-H_6 showed much smaller k_{app} values compared to those of R72A-H_6, R72E-H_6, and Y71A-H_6. On the other hand, Y71F-H_6 showed distinctly large k_{app} values at pH 5.0, about 7–8 times larger than the corresponding values of WT-Zmb_{561}-H_6 and 3–4 times larger than those of R72D-H_6, R72E-H_6, Y71A-H_6. Thus, from the data in Fig. 4A and Table S8, we can conclude that the substitutions of Arg^{72} (with Ala or Asp) and Tyr^{71} (with Ala or Phe) caused a significant suppression of the characteristic pH-dependent time-lag upon the electron acceptance from AsA, leading to the faster electron acceptance from AsA at acidic pH. In the case of the substitution of Tyr^{71} with Phe, there was actually a significant acceleration of the electron transfer from AsA (Table S8). These observations indicated some important roles of Tyr^{71} for the electron transfer from bound AsA.

Stopped-flow analyses of the Y71A/K83A double mutant The Y71A/K83A double mutant showed fast electron accepting reactions from AsA irrespective of pH (Fig. 4Bb, Table S9). It was noteworthy that there was no apparent initial delay even at pH 5.0 (Fig. 4Bb). This behavior was very similar to those of Y71A-H_6 and R72A-H_6 mutants (Fig. 4A). These results confirmed that the significant lowering of the electron accepting ability caused by the K83A mutation (29) was rescued by introducing the second mutation of Y71A. However, the original pH-dependency as found for wild-type Zmb_{561}-H_6 (Fig. 4Aa) [or in WT-Zmb_{561} (29) and adrenal CG cytochrome b_{561} (17)] was lost almost completely for its compensation.

TABLE 1. Redox potentials of Zmb_{561} and effects of site-specific mutations on the redox properties in comparison with those of bovine adrenal CG cytochrome b_{561}.

Cytochromes	Apparent midpoint potential (mV)	Slope[a]	Estimated higher midpoint potential[b] (mV)	Estimated lower midpoint potential[b] (mV)
WT-Zmb_{561}	+65.6	46.4	+118.9	+11.3
WT-Zmb_{561}-H_6	+64.0	46.3	+118.2	+8.5
R72A-H_6	+76.5	41.3	+119.9	+27.3
R72D-H_6[c]	ND	ND	ND	ND
R72E-H_6	+52.7	49.1	+110.5	−6.2
R72K-H_6	+62.7	51.9	+126.2	−1.3
Y71A-H_6	+41.8	39.2	+83.8	0.0
Y71F–H_6	+10.6	61.7	+76.7	−74.7
K83A/Y71A	+37.7	36.4	+78.3	−0.6
K83A[d]	+44.8	41.5	+93.0	−4.4
Bovine CG b_{561}[e]	+125	–	+170	+60
Bovine CG b_{561}[f]	+128	–	+170	+70

[a] Slope values were defined as variables during the fitting procedure using a single sigmoidal function and are, therefore, corresponding to the slope of the curvature.
[b] For the curve-fitting procedure using two independent sigmoidal functions, slope value for each sigmoidal function was fixed as 25.619 and is, therefore, not indicated.
[c] Due to the instability of the purified protein at room temperature, reliable redox potential measurements could not be performed and, therefore, these values were not determined (ND).
[d] From Nakanishi et al. (29) for Zmb_{561} without the His-tag moiety.
[e] From Apps et al. (53) for the purified form obtained from bovine adrenal gland.
[f] From Takeuchi et al. (16) for the purified form obtained from bovine adrenal gland CG.

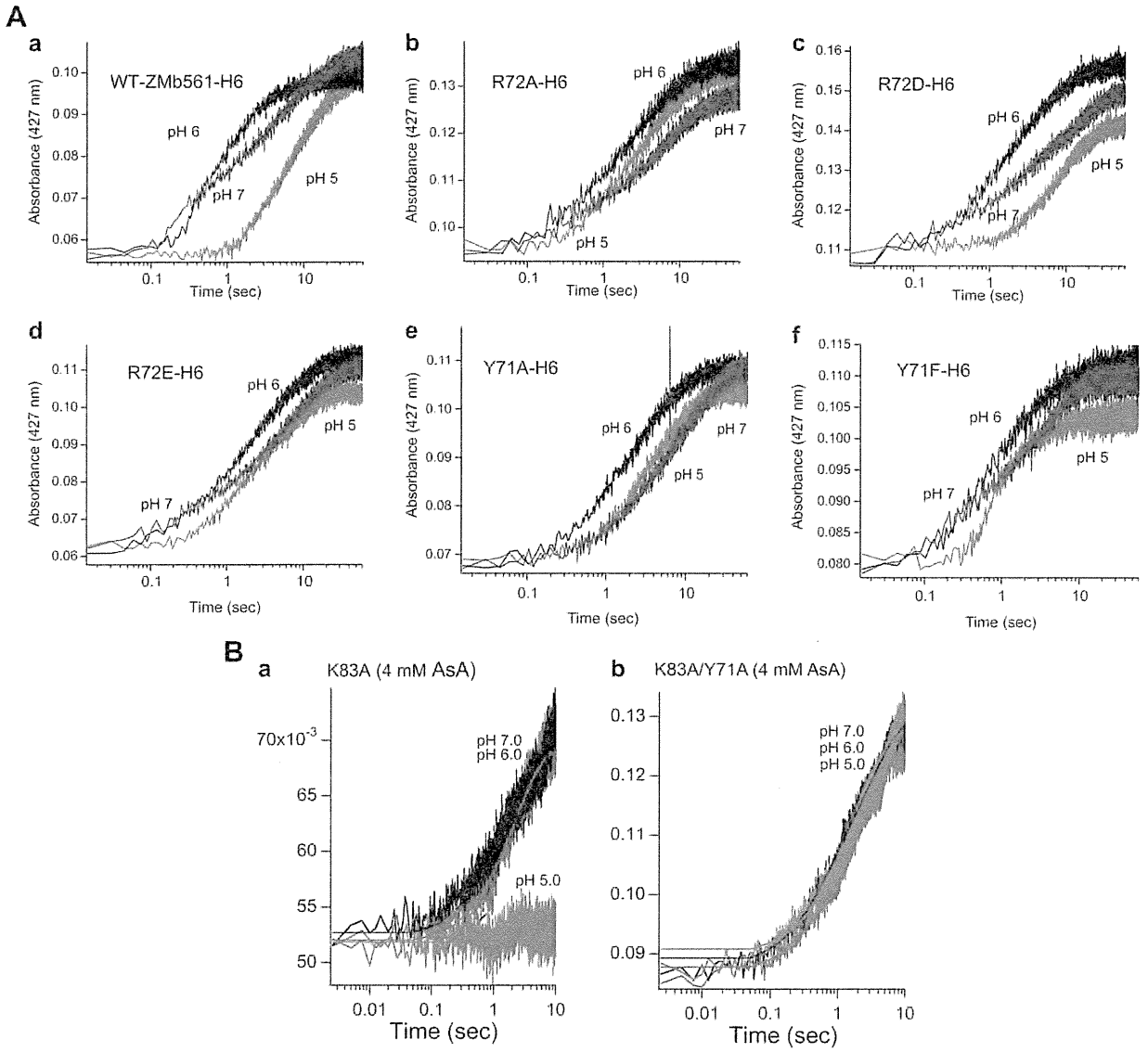

FIG. 4. (A) Stopped-flow analyses of the electron transfer from AsA for the purified WT-Zmb_{561}-H_6, its R72 mutants (R72A-H_6, R72D-H_6, R72E-H_6), and Y71 mutants (Y71A-H_6, Y71F-H_6) measured at three different pH. (B) Stopped-flow analyses of the electron transfer from AsA for the purified WT-Zmb_{561}, K83A, and K83A/Y71A mutants measured at three different pH. (A) The electron accepting reactions of oxidized WT-Zmb_{561}-H_6 (a) [and its site-directed mutants; R72A-H_6 (b), R72D-H_6 (c), R72E-H_6 (d), Y71A-H_6 (e) and Y71F-H_6 (f)] (final, 1 μM) from AsA (final, 2 mM) were measured at 427 nm and at three different pH (pHs 5.0, 6.0, and 7.0) by stopped-flow spectrometry using two solution mixing system with a 1:1 volume ratio. The absorbance changes were plotted against time in a logarithmic scale. (B) The electron accepting reactions of oxidized K83A (a) and K83A/Y71A (b) mutants (final, 1 μM) from AsA (final, 4 mM) were measured at three different pH (pHs 5.0, 6.0, and 7.0). Other conditions including buffer conditions are the same as in panel A.

DISCUSSION

Electrochemistry of AsA and its relation to the electron transfer mechanism to the heme center of cytochrome b_{561} Since AsA has two acidic protons (pK_{a1} = 4.04 and pK_{a2} = 11.34) (38), three species, i.e., ascorbic acid (H_2AsA), ascorbate monoanion ($HAsA^-$), and ascorbate dianion (AsA^{2-}), are present in neutral solution with the monoanion form as a predominant species. For ascorbate free radicals, monoanion form (MDA^-) is a predominant species under physiological conditions (23,38,39). Since the monoanion form ($HAsA^-$) is not a good electron donor and the scarce dianion form (AsA^{2-}) is a much powerful electron donor, it was postulated that adrenal CG cytochrome b_{561} has such a molecular mechanism to withdraw a proton from the monoanion form to facilitate electron transfer to its oxidized heme (concerted H^+/e^- transfer mechanism) (23). We extended the model to include an imidazole group of the cytosolic heme axial His ligand as a site for the proton acceptance (30). Our previous studies on Zmb_{561} (31,40) showed that the concerted H^+/e^- transfer mechanism is operative in plant cytochrome b_{561} as well.

For a better understanding of the efficient electron transfer reaction of Zmb_{561} from AsA based on the concerted H^+/e^- transfer mechanism, we may categorize conserved amino acid residues near the AsA-binding site by considering their putative mechanistic roles; namely, (i) residues responsible for helping the approach of AsA to the AsA-binding site and for its recognition, (ii) residues responsible for the stabilization of AsA at the AsA-binding site, which may promote the electron transfer by providing a route to the oxidized heme, (iii) residues responsible for withdrawing and transferring a proton from C2–OH group of AsA, which may also provide a route for the electron transfer, and (iv) residues

responsible for expelling MDA radical from the AsA-binding site to prevent a reverse electron flow from the reduced heme center.

Our previous site-specific chemical modification studies on adrenal CG cytochrome b_{561} suggested the importance of conserved Lys^{85} (corresponding to Lys^{83} of WT-Zmb_{561}-H$_6$) for the quick electron acceptance from AsA (15,16). More recent studies on WT-Zmb_{561} and WT-Zmb_{561}-H$_6$ (31,40) indicated that Lys^{83} had a similar high reactivity toward DEPC and such a specific DEPC-modification caused a significant retardation of the electron transfer from AsA. Mechanistic role(s) of this positively-charged residue was further analyzed by site-specific mutants, K83A, K83D, and K83E (29). Stopped-flow analyses showed that the initial time-lag phase for these mutants was much longer than that of WT-Zmb_{561}, causing a significant retardation of the electron transfer (29). One may propose that the initial lag-phase of the wild-type protein is due to the presence of a resting inactive state, which must first be reactivated. Although we cannot discard such a possibility completely, this view is not consistent with the results for the three Lys^{83} mutants (29), which indicated further extension of the initial lag-phase. Therefore, the initial lag-phase might be directly related to the binding process of AsA, being consistent with the notion that a positive charge of Lys^{83} would have an electrostatic interaction with a negatively-charged AsA molecule (17). Thus, Lys^{83} should be classified as group A.

DEPC-treatments of WT-Zmb_{561}-H$_6$ and four site-specific mutants (Y71A-H$_6$, R72A-H$_6$, R72D-H$_6$, and R72E-H$_6$) (40) caused similar inhibitory effects on their electron acceptance from AsA as found for WT-Zmb_{561} (31). DEPC-treatment of K83A mutant also showed a similar inhibition (40), in which only heme axial His residue(s) were potential major modification sites. These results suggested that the specific *N*-carbethoxylation of the heme axial His residue(s) was a major cause of the inhibition of electron acceptance from AsA. Thus, based on the concerted H$^+$/e$^-$ transfer mechanism at the cytosolic heme center (30), we conclude that His^{86} could be classified as group C.

Possible mechanistic roles of Arg^{72} Previously, Arg^{72} was proposed as an important residue for the interaction with AsA because of its positive charge and its high conservation (32). In the past, several X-ray crystal structures for AsA-bound enzymes, including ascorbate peroxidases (41), hyaluronate lyase (42), and myrosinase (43), were reported. In all of these structures, a conserved Arg residue has essential roles for the binding of AsA at their active sites (44), in which side-chains of the Arg residues were interacted with the 2-O and 3-O atoms (41), 1-O and 2-O atoms (42), 1-O and 2-O atoms (43) of the bound AsA *via* hydrogen bonding, respectively. Further, in the engineered AsA-binding site of cytochrome *c* peroxidase by mimicking ascorbate peroxidase, an introduced Arg residue was found to form a hydrogen bond (45). Indeed, a site-directed mutagenesis study on mouse recombinant CG cytochrome b_{561} in the yeast membrane fraction indicated that mutation of Arg^{72} to Ala abolished the high affinity heme reduction by AsA (32). Further, site-directed mutagenesis studies on Lcytb showed that mutation of Arg^{67} (corresponding to Arg^{72}) to Ala resulted in an almost complete loss of the activity in the yeast cell-surface ferric reductase assay (25). These pieces of evidence seemed to suggest that Arg^{72} could be categorized as group A or group B. However, our present results on the Arg^{72} mutants did not support these observations and were not consistent with the notion that Arg^{72} provides an electrostatic interaction(s) with AsA to facilitate the electron transfer from it. Removal of the positive charge by substitution with Ala (R72A) or conversion to a negatively-charged residue by substitution with Asp (R72E) did not cause any retardation (or lowering) of the electron transfer from AsA at all at a neutral pH, when analyzed with stopped-flow spectrometry. More interestingly, the initial time-lag observed for adrenal CG cytochrome b_{561} (17) and WT-Zmb_{561} (29) (and in the present study for WT-Zmb_{561}-H$_6$) observed at an acidic pH was completely lost in these mutants, just in an opposite direction of that seen for the Lys^{83} mutants, although for the R72D mutant the initial time-lag was somewhat conserved and the apparent rate constants for the electron acceptance from AsA were still slower at pH 5.0 (Table S8). These results suggest that Arg^{72} has a clearly different mechanistic role(s) from that of Lys^{83} in the electron accepting reaction from AsA. At an acidic pH, major HAsA$^-$ and minor H$_2$AsA forms are in equilibrium and, somehow, Arg^{72} stabilizes the bound AsA molecule to shift the equilibrium in favoring the H$_2$AsA form, as depicted in Fig. 5. In this stabilized structure, a proton (of the 2-OH group) could not be removed from AsA by His^{86} *via* concerted H$^+$/e$^-$ transfer mechanism (Fig. 5) and, therefore, a significant initial time-lag might be observed. However, substitution of the positive side-chain with a neutral or a negative group (i.e., R72A and R72E mutants) might cause an easier release of a proton from the bound AsA leading to a faster electron transfer from AsA to the heme iron. In the case of R72D mutant, however, there was no such promoting effect, possibly due to a shorter side-chain of Asp^{72} than that of Glu^{72} of R72E.

If so, what is a mechanistic role(s) of the stabilization of the bound AsA by Arg^{72}? The most-likely explanation is that Arg^{72} may have a role to destabilize the binding of MDA monoanion (MDA$^-$) radical at the AsA-binding site to prevent a reverse electron flow from the reduced heme center (Fig. 5). Although both MDA monoanion (MDA$^-$) radical and ascorbate monoanion (HAsA$^-$) has a negative charge, fine discrimination might be possible since the former has one unpaired electron spread over a highly conjugated tricarbonyl system (39) and is presumably much planar than the latter (Fig. 5). It is quite reasonable to consider that adrenal CG cytochrome b_{561} might also have this kind of molecular mechanism for expelling MDA radical from AsA-binding site. Since there are sufficient amounts of intravesicular (~10 mM) and cytosolic

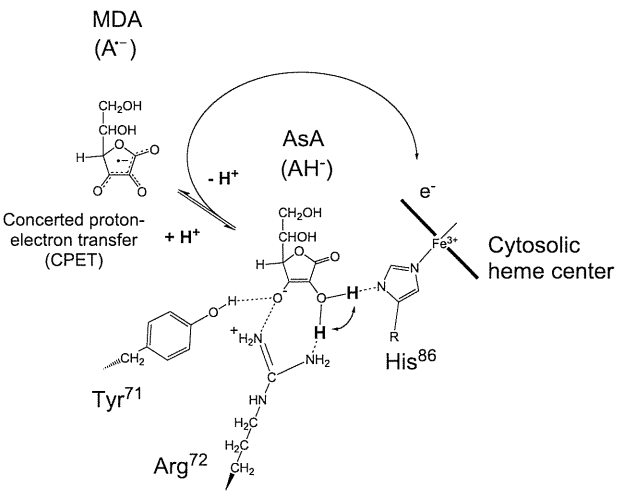

FIG. 5. Possible roles of Arg^{72}, Tyr^{71} and His^{86} in the electron transfer reaction from AsA to the cytosolic heme center of Zmb_{561}. We postulated that both Arg^{72} and Tyr^{71} have strong hydrogen bonding (or electrostatic) interactions with the bound AsA at the putative AsA-binding site. This will cause slowdown of the proton release from the bound AsA, resulting in retardation of the electron transfer from AsA to the cytosolic heme center, particularly at acidic pH. Then, release of a proton from the bound AsA would be promoted by His^{86} *via* concerted H$^+$/e$^-$ transfer mechanism. There might be a movement (or conformational readjustment) of the bound AsA before proceeding to the next step. The physiological role of Arg^{72} and Tyr^{71} might be an expelling of MDA radical from the AsA-binding site to prevent a reverse electron transfer. Lys^{83} was omitted from the scheme for the simplicity.

(~5 mM) AsA in adrenal chromaffin cells and, therefore, cytochrome b_{561} is almost in the fully-reduced state. Accordingly, prevention of the reverse electron transfer to MDA radical on the cytosolic side might be a primary importance. Such a molecular mechanism may be distributed among plant cytochromes b_{561} as well. In this case, Arg^{72} might be classified as group D rather than group B.

Possible mechanistic roles of Tyr^{71} For the two Tyr^{71} mutants, we did observe some significant influences of the mutations on the final heme reduction level with AsA, but in a different way. Y71A-H_6 showed a lower heme reduction level than those of WT-Zmb_{561}-H_6. On the other hand, Y71F-H_6 mutant showed a very high reduction level at pH 5.0, whereas at pH 6.0 and 7.0 its reduction level was much lower (45–50%) than that of WT-Zmb_{561}-H_6. Stopped-flow analysis of Y71A-H_6 mutant did not show any retardation upon the electron acceptance from AsA at a neutral pH. Importantly, again, the characteristic initial time-lag was almost absent at acidic pH. In the case of Y71F-H_6 mutant, all the steps of the electron transfer from AsA seemed to be accelerated, particularly at acidic pH. These results indicated that the mechanistic role of Tyr^{71} might be also very complex.

The EPR spectra of oxidized Y71A mutant measured at 5 and 15 K (Fig. S8) showed that the low-spin species with HALS character, which has been assigned to the cytosolic heme center, was actually composed of two species with slightly different g_z values (g_z = 3.70 and 3.59). The latter g_z-signal (g_z = 3.59) was not observed in those of oxidized WT-Zmb_{561} and K83A mutant measured at 5 and 15 K (29). On the other hand, the other low-spin species (g_z = 3.15) assignable to the intravesicular heme center seemed to remain intact. These results suggested that the coordination structure of the cytosolic heme center was slightly perturbed upon the mutation of Tyr^{71} and such an alteration might become apparent only at low temperatures. Thus, it is tempting to propose that Tyr^{71} contributes to a structural role for the stabilization around the cytosolic heme center by considering its rather high conservation in many cytochromes b_{561} (13,14). The appearance of the g_z = 2.90 species (7,46) may indicate that such a decrease in the stability around the cytosolic heme center could be propagated further to the overall stability of Zmb_{561} molecule.

Recently, however, this classical view was challenged as that the g_z = 3.7 signal was assignable to the low-potential intravesicular heme and *vice versa* (47–49). In this new topological model, however, there was a difficulty that the transmembrane electron transport occurs against ~100 mV gradient of the redox potentials of the two heme centers (47). Indeed, in a more recent study employing *Arabidopsis* cytochrome b_{561} being expressed in both *P. pastoris* and *Escherichia coli* cells and DEPC reagent, Cenacchi *et al.* concluded that the AsA-binding site is located near the low-potential heme (i.e., the g_z = 3.7 heme) and the other ferric-chelates reduction site is close to the high-potential heme (i.e., the g_z = 3.15 heme) (50). Accordingly, in the following discussion, we take the classical view of the heme assignments; however, even if our assignments were wrong, it would not affect the final conclusion.

Detailed analysis on the stopped-flow experiments suggested that Tyr^{71} has an additional role other than the structural one. Its possible role may be the destabilization of a bound MDA radical and expelling it from the AsA-binding site, similar to that of Arg^{72}. In our proposed scenario, the phenol-OH group of Tyr^{71} in collaboration with Arg^{72} might have specific interactions with the bound AsA in favoring the H_2AsA form (Fig. 5) and, accordingly, release of the 2-OH proton from the bound AsA might be inhibited at a lower pH. Indeed, such an example for this kind interaction between a Tyr residue and a bound AsA is proposed for a plant heme oxygenase (44). For a planar MDA radical without the 2-OH group [i.e., monoanion form (MDA^-)], Tyr^{71} would not have any preference and the MDA radial might be expelled from the AsA-binding site and, therefore, the reverse electron transfer would be inhibited. Substitution of Tyr^{71} with Ala will abolish such specific interactions to stabilize AsA, causing a prompt release of the proton from the bound AsA, leading to a faster electron transfer from the AsA to the heme iron. Further, conversion to the more hydrophobic environments upon the substitution of Tyr^{71} with Ala would destabilize a negatively-charged AsA in its binding site. This interpretation might be supported by the observation that Y71A-H_6 mutant showed a very similar property with that of R72A-H_6 mutant. Substitution of Tyr^{71} with a more hydrophobic Phe would enhance such a promoting effect by changing the nature of the AsA-binding pocket, which was verified in our present study. The significant lowering of the midpoint potential of the lower potential heme of Y71F-H_6 mutant (Table 1) might be a direct effect of such changes.

More convincing evidence was obtained from the stopped-flow studies on the K83A/Y71A double mutant. The significant lowering of electron accepting ability from AsA at pH 5.0 caused by the K83A mutation (29) (Fig. 4Ba) was rescued by the introduction of a second mutation of Y71A (Fig. 4Bb). However, it is noteworthy that the original pH-dependency observed for WT-Zmb_{561}-H_6 (Fig. 4Aa) [which was further enhanced for K83A mutant (29)] was completely lost for its compensation. The resulting behavior of K83A/Y71A double mutant was very similar to that of Y71A-H_6 mutant both in the stopped-flow analysis (Fig. 4Ae) and in the redox potential measurement (Table 1).

From all these pieces of evidence, we propose that both Arg^{72} and Tyr^{71} have similar physiological roles for expelling MDA radical from the AsA-binding site (by stabilizing AsA molecule) to prevent a back-flow of electron equivalents from the reduced heme center on the cytosolic side (Fig. 5). Accordingly, both Arg^{72} and Tyr^{71} could be classified as group D rather than group B.

It has been shown that electron transfer across the adrenal CG membranes can create a membrane potential (51). Similar energetic considerations on the plant tonoplast would argue that the membrane potential might also affect the rate of transmembrane electron transfer as well. The proton gradient (inside-positive) across the membranes (membrane potential included) is supposed to favor the electron transfer in inward direction both in adrenal CG membranes (52) and in tonoplast membranes. However, in a certain case where the proton gradient was dissipated by acidification of cytosol, the electron equivalents accommodated in the intravesicular AsA would be released by the outward transmembrane electron flow *via* cytochrome b_{561}. In this sense, the mechanistic role of the conserved Arg^{72} and Tyr^{71} integrated in cytochrome b_{561} proteins might be very intriguing as a very suitable pH-sensitive switch. To verify our present proposal, however, a detailed structural data based on the X-ray crystallographic study might be highly necessary.

Supplementary material related to this article can be found at http://dx.doi.org/10.1016/j.jbiosc.2012.11.013.

ACKNOWLEDGMENTS

This work was supported by Grants-in-Aid for Scientific Research on Priority Areas (System Cell Engineering by Multi-scale Manipulation; 18048030 and 20034034 to M. T.) from the Japanese Ministry of Education, Culture, Sports, Science and Technology and by Grant-in-Aid for Scientific Research (C) (22570142) from Japan Society for the Promotion of Science.

References

1. **Trost, P., Bèrczi, A., Sparla, F., Sponza, G., Marzadori, B., Asard, H., and Pupillo, P.:** Purification of cytochrome b_{561} from bean hypocotyls plasma

membrane. Evidence for the presence of two heme centers, Biochim. Biophys. Acta, **1468**, 1–5 (2000).
2. **Bérczi, A., Lüthje, S., and Asard, H.:** *b*-type cytochromes in plasma membranes of *Phaseolus vulgaris* hypocotyls, *Arabidopsis thaliana* leaves, and *Zea mays* roots, Protoplasma, **217**, 50–55 (2001).
3. **Asard, H., Kapila, J., Verelst, W., and Bérczi, A.:** Higher-plant plasma membrane cytochrome b_{561}: a protein in search of a function, Protoplasma, **217**, 77–93 (2001).
4. **Preger, V., Pesaresi, A., Pupillo, P., and Trost, P.:** Ascorbate-independent electron transfer between cytochrome b_{561} and a 27 kDa ascorbate peroxidase of bean hypocotyls, Protoplasma, **217**, 137–145 (2001).
5. **Kent, U. M. and Fleming, P. J.:** Purified cytochrome b_{561} catalyzes transmembrane electron transfer for dopamine β-hydroxylase and peptidyl glycine α-amidating monooxygenase activities in reconstituted systems, J. Biol. Chem., **262**, 8174–8178 (1987).
6. **Perin, M. S., Fried, V. A., Slaughter, C. A., and Südhof, T. C.:** The structure of cytochrome b_{561}, a secretory vesicle-specific electron transport protein, EMBO J., **7**, 2697–2703 (1988).
7. **Tsubaki, M., Nakayama, M., Okuyama, E., Ichikawa, Y., and Hori, H.:** Existence of two heme B centers in cytochrome b_{561} from bovine adrenal chromaffin vesicles as revealed by a new purification procedure and EPR spectroscopy, J. Biol. Chem., **272**, 23206–23210 (1997).
8. **Asard, H., Terol-Alcayde, J., Preger, V., Del Favero, J., Verelst, W., Sparla, F., Pérez-Alonso, M., and Trost, P.:** *Arabidopsis thaliana* sequence analysis confirms the presence of cyt *b*-561 in plants: evidence for a novel protein family, Plant Physiol. Biochem., **38**, 905–912 (2000).
9. **Mckie, A. T., Barrow, D., Latunde-Dada, G. O., Rolfs, A., Sager, G., Mudaly, E., Mudaly, M., Richardson, C., Barlow, D., Bomford, A., and other 6 authors:** An iron-regulated ferric reductase associated with the absorption of dietary iron, Science, **291**, 1755–1759 (2001).
10. **Zhang, D.-L., Su, D., Bérczi, A., Vargas, A., and Asard, H.:** An ascorbate-reducible cytochrome b_{561} is localized in macrophage lysosomes, Biochim. Biophys. Acta, **1760**, 1903–1913 (2006).
11. **Bérczi, A. and Asard, H.:** Expression and purification of the recombinant mouse tumor suppressor cytochrome b_{561} protein, Acta Biol. Szeged., **52**, 257–265 (2008).
12. **Recuenco, M. C., Fujito, M., Rahman, M. M., Sakamoto, Y., Takeuchi, F., and Tsubaki, M.:** Functional expression and characterization of human *101F6* protein, a homologue of cytochrome b_{561} and a candidate tumor suppressor gene product, BioFactors, **34**, 219–230 (2009).
13. **Tsubaki, M., Takeuchi, F., and Nakanishi, N.:** Cytochrome b_{561} protein family: expanding roles and versatile transmembrane electron transfer abilities as predicted by a new classification system and protein sequence motif analyses, Biochim. Biophys. Acta, **1753**, 174–190 (2005).
14. **Okuyama, E., Yamamoto, R., Ichikawa, Y., and Tsubaki, M.:** Structural basis for the electron transfer across the chromaffin vesicle membranes catalyzed by cytochrome b_{561}: analyses of cDNA nucleotide sequences and visible absorption spectra, Biochim. Biophys. Acta, **1383**, 269–278 (1998).
15. **Tsubaki, M., Kobayashi, K., Ichise, T., Takeuchi, F., and Tagawa, S.:** Diethyl pyrocarbonate-modification abolishes fast electron accepting ability of cytochrome b_{561} from ascorbate but does not influence on electron donation to monodehydroascorbate radical: distinct roles of two heme centers for electron transfer across the chromaffin vesicle membranes, Biochemistry, **39**, 3276–3284 (2000).
16. **Takeuchi, F., Kobayashi, K., Tagawa, S., and Tsubaki, M.:** Ascorbate inhibits the carbethoxylation of two histidyl and one tyrosyl residues indispensable for the transmembrane electron transfer reaction of cytochrome b_{561}, Biochemistry, **40**, 4067–4076 (2001).
17. **Takigami, T., Takeuchi, F., Nakagawa, M., Hase, T., and Tsubaki, M.:** Stopped-flow analyses on the reaction of ascorbate with cytochrome b_{561} purified from bovine chromaffin vesicle membranes, Biochemistry, **42**, 8110–8118 (2003).
18. **Kobayashi, K., Tsubaki, M., and Tagawa, S.:** Distinct roles of two heme centers for transmembrane electron transfer in cytochrome b_{561} from bovine adrenal chromaffin vesicles as revealed by pulse radiolysis, J. Biol. Chem., **273**, 16038–16042 (1998).
19. **Asard, H., Venken, M., Caubergs, R., Reijnders, W., Oltmann, F. L., and De Greef, J. A.:** *b*-Type cytochromes in higher plant plasma membranes, Plant Physiol., **90**, 1077–1083 (1989).
20. **Griesen, D., Su, D., Bérczi, A., and Asard, H.:** Localization of an ascorbate-reducible cytochrome b_{561} in the plant tonoplast, Plant Physiol., **134**, 726–734 (2004).
21. **Nanasato, Y., Akashi, K., and Yokota, A.:** Co-expression of cytochrome b_{561} and ascorbate oxidase in leaves of wild watermelon under drought and high light conditions, Plant Cell Physiol., **46**, 1515–1524 (2005).
22. **Bérczi, A., Su, D., and Asard, H.:** An *Arabidopsis* cytochrome b_{561} with *trans*-membrane ferrireductase capability, FEBS Lett., **581**, 1505–1508 (2007).
23. **Njus, D. and Kelley, P. M.:** The secretory-vesicle ascorbate-regenerating system: a chain of concerted H^+/e^--transfer reactions, Biochim. Biophys. Acta, **1144**, 235–248 (1993).
24. **Vargas, J. D., Herpers, B., Mckie, A. T., Gledhill, S., McDonnell, J., van der Heuvel, M., Davies, K. E., and Ponting, C. P.:** Stromal cell-derived receptor 2 and cytochrome b_{561} are functional ferric reductase, Biochim. Biophys. Acta, **1651**, 116–123 (2003).
25. **Su, D. and Asard, H.:** Three mammalian cytochrome b_{561} are ascorbate-dependent ferrireductases, FEBS J., **273**, 3722–3734 (2006).
26. **Bérczi, A., Caubergs, R. J., and Asard, H.:** Partial purification and characterization of an ascorbate-reducible *b*-type cytochrome from the plasma membrane of *Arabidopsis thaliana* leaves, Protoplasma, **221**, 47–56 (2003).
27. **Verelst, W., Kapila, J., de Almeida Engler, J., Stone, J. M., Caubergs, R. J., and Asard, H.:** Tissue-specific expression and developmental regulation of cytochrome b_{561} genes in *Arabidopsis thaliana* and *Raphanus sativus*, Physiol. Plant., **120**, 312–318 (2004).
28. **Rahman, M. M., Nakanishi, N., Takigami, T., Hase, T., Park, S.-Y., and Tsubaki, M.:** Purification and biochemical analysis of *Zea mays* cytochrome b_{561} heterologously expressed in *Pichia pastoris*, pp. 108–112, in: MHS2007. International Symposium on Micro-NanoMechatronics and Human Science, 2007. IEEE, Nagoya (2007).
29. **Nakanishi, N., Rahman, M. M., Sakamoto, Y., Takigami, T., Kobayashi, K., Hori, H., Hase, T., Park, S.-Y., and Tsubaki, M.:** Importance of conserved Lys83 residue of *Zea mays* cytochrome b_{561} for ascorbate-specific transmembrane electron transfer as revealed by site-directed mutagenesis studies, Biochemistry, **48**, 10665–10678 (2009).
30. **Nakanishi, N., Takeuchi, F., and Tsubaki, M.:** Histidine cycle mechanism for the concerted proton/electron transfer from ascorbate to the cytosolic heme *b* center of cytochrome b_{561}: a unique machinery for the biological transmembrane electron transfer, J. Biochem., **142**, 553–560 (2007).
31. **Nakanishi, N., Rahman, M. M., Sakamoto, Y., Miura, M., Takeuchi, F., Park, S.-Y., and Tsubaki, M.:** Inhibition of electron acceptance from ascorbate by the specific *N*-carbethoxylations of maize cytochrome b_{561}: a common mechanism for the transmembrane electron transfer in cytochrome b_{561} protein family, J. Biochem., **146**, 857–866 (2009).
32. **Bérczi, A., Su, D., Lakshminarasimhan, M., Vargas, A., and Asard, H.:** Heterologous expression and site-directed mutagenesis of an ascorbate-reducible cytochrome b_{561}, Arch. Biochem. Biophys., **443**, 82–92 (2005).
33. **Lakshminarasimhan, M., Bérczi, A., and Asard, H.:** Substrate-dependent reduction of a recombinant chromaffin granule Cyt-b_{561} and its R72A mutant, Acta Biol. Szeged., **50**, 61–65 (2006).
34. **Bérczi, A. and Asard, H.:** Characterization of an ascorbate-reducible cytochrome b_{561} by site-directed mutagenesis, Acta Biol. Szeged., **50**, 55–59 (2006).
35. **Laemmli, U. K.:** Cleavage of structural proteins during the assembly of the head of bacteriophage T_4, Nature, **227**, 680–685 (1970).
36. **Dutton, P. L.:** Redox potentiometry: determination of midpoint potentials of oxidation-reduction components of biological electron-transfer systems, Methods Enzymol., **54**, 411–435 (1978).
37. **Walker, F. A., Huynh, B. H., Scheidt, W. R., and Osvath, S. R.:** Models of the cytochromes *b*. Effect of axial ligand plane orientation on the EPR and Mössbauer spectra of low-spin ferrihemes, J. Am. Chem. Soc., **108**, 5288–5297 (1986).
38. **Williams, N. H. and Yandell, J. K.:** Outer-sphere electron-transfer reactions of ascorbate anions, Aust. J. Chem., **35**, 1133–1144 (1982).
39. **Laroff, G. P., Fessenden, R. W., and Schuler, R. H.:** The electron spin resonance spectra of radical intermediates in the oxidation of ascorbic acid and related substances, J. Am. Chem. Soc., **94**, 9062–9073 (1972).
40. **Rahman, M. M., Nakanishi, N., Fujito, M., Miura, M., Hase, T., Park, S.-Y., Hori, H., and Tsubaki, M.:** Inhibition of the electron transfer of plant cytochrome b_{561} by the modification with diethylpyrocarbonate: in search of a common mechanism for the transmembrane electron transfer from ascorbate, pp. 157–162, in: MHS2008. International Symposium on Micro-Nano-Mechatronics and Human Science, 2008. IEEE, Nagoya (2008).
41. **Sharp, K. H., Mewies, M., Moody, P. C. E., and Raven, E. L.:** Crystal structure of the ascorbate peroxidase–ascorbate complex, Nat. Struct. Biol., **10**, 303–307 (2003).
42. **Li, S., Taylor, K. B., Kelly, S. J., and Jedrzejas, M. J.:** Vitamin C inhibits the enzymatic activity of *Streptococcus pneumoniae* hyaluronate lyase, J. Biol. Chem., **276**, 15125–15130 (2001).
43. **Burmeister, W. P., Cottaz, S., Rollin, P., Vasella, A., and Henrissat, B.:** High resolution X-ray crystallography shows that ascorbate is a cofactor for myrosinase and substrates for the function of the catalytic base, J. Biol. Chem., **275**, 39385–39393 (2000).
44. **Linley, P. J., Landsberger, M., Kohchi, T., Cooper, J. B., and Terry, M. J.:** The molecular basis of heme oxygenase deficiency in the *pcd1* mutant of pea, FEBS J., **273**, 2594–2606 (2006).
45. **Murphy, E. J., Metcalfe, C. L., Basran, J., Moody, P. C. E., and Raven, E. L.:** Engineering the substrate specificity and reactivity of a heme protein: creation of an ascorbate binding site in cytochrome *c* peroxidase, Biochemistry, **47**, 13933–13941 (2008).
46. **Ludwiczek, S., Rosell, F. I., Ludwiczek, M. L., and Mauk, A. G.:** Recombinant expression and initial characterization of the putative human enteric ferric reductase Dcytb, Biochemistry, **47**, 753–761 (2008).

47. **Kamensky, Y., Liu, W., Tsai, A.-L., Kulmacz, R. J., and Palmer, G.:** The axial ligation and stoichiometry of heme centers in adrenal cytochrome b_{561}, Biochemistry, **46**, 8647–8658 (2007).
48. **Liu, W., Rogge, C. E., da Silva, G. F. Z., Shinkarev, V. P., Tsai, A.-L., Kamensky, Y., Palmer, G., and Kulmacz, R. J.:** His92 and His110 selectively affect different heme centers of adrenal cytochrome b_{561}, Biochim. Biophys. Acta, **1777**, 1218–1228 (2008).
49. **Desmet, F., Bérczi, A., Zimányi, L., Asard, H., and Van Doorslaer, S.:** Axial ligation of the high-potential heme center in an *Arabidopsis* cytochrome b_{561}, FEBS Lett., **585**, 545–548 (2011).
50. **Cenacchi, L., Busch, M., Schleidt, P. G., Müller, F. G., Stumpp, T. V. M., Mäntele, W., Trost, P., and Lancaster, C. R. D.:** Heterologous production and characterisation of two distinct dihaem-containing membrane integral cytochrome b_{561} enzymes from *Arabidopsis thaliana* in *Pichia pastoris* and *Escherichia coli* cells, Biochim. Biophys. Acta, **1818**, 679–688 (2012).
51. **Harnadek, G. J., Callahan, R. E., Barone, A. R., and Njus, D.:** An electron transfer dependent membrane potential in chromaffin-vesicle ghosts, Biochemistry, **24**, 384–389 (1985).
52. **Harnadek, G., Ries, E. A., Farhat, A., and Njus, D.:** 5-Methylphenazinium methylsulfate mediates cyclic electron flow and proton gradient dissipation in chromaffin-vesicle membranes, J. Biol. Chem., **265**, 18135–18141 (1990).
53. **Apps, D. K., Boisclair, M. D., Gavine, F. S., and Pettigrew, G. W.:** Unusual redox behaviour of cytochrome *b*-561 from bovine chromaffin granule membranes, Biochim. Biophys. Acta, **764**, 8–16 (1984).

THE JOURNAL OF BIOLOGICAL CHEMISTRY VOL. 288, NO. 51, pp. 36351–36360, December 20, 2013

IQGAP1 Protein Regulates Nuclear Localization of β-Catenin via Importin-β5 Protein in Wnt Signaling*

Received for publication, September 18, 2013, and in revised form, November 4, 2013 Published, JBC Papers in Press, November 6, 2013, DOI 10.1074/jbc.M113.520528

Toshiyasu Goto[‡], Atsushi Sato[‡], Shungo Adachi[§], Shun-ichiro Iemura[§], Tohru Natsume[§], and Hiroshi Shibuya[‡1]

From the [‡]Department of Molecular Cell Biology, Medical Research Institute, Tokyo Medical and Dental University, Bunkyo-ku, Tokyo 113-8510 and the [§]Molecular Profiling Research Center for Drug Discovery, National Institute of Advanced Industrial Science and Technology, 2-4-7 Aomi, Koto-ku, Tokyo 135-0064, Japan

Background: The molecular mechanisms underlying the β-catenin nuclear localization remain unclear.
Results: IQGAP1 is a regulator of β-catenin nuclear localization.
Conclusion: Importin-β5 and Ran contribute to the nuclear localization of β-catenin.
Significance: Novel molecular mechanisms were found in Wnt signaling.

In the canonical Wnt signaling pathway, the translocation of β-catenin is important for the activation of target genes in the nucleus. However, the molecular mechanisms underlying its nuclear localization remain unclear. In the present study, we found IQGAP1 to be a regulator of β-catenin function via importin-β5. In *Xenopus* embryos, depletion of IQGAP1 reduced Wnt-induced nuclear accumulation of β-catenin and expression of Wnt target genes during early embryogenesis. Depletion of endogenous importin-β5 associated with IQGAP1 also reduced expression of Wnt target genes and the nuclear localization of IQGAP1 and β-catenin. Moreover, a small GTPase, Ran1, contributes to the nuclear translocation of β-catenin and the activation of Wnt target genes. These results suggest that IQGAP1 functions as a regulator of translocation of β-catenin in the canonical Wnt signaling pathway.

β-Catenin acts as an indispensable component in canonical Wnt signaling (1, 2). In the Wnt off-state, β-catenin levels are kept low through the interaction with Axin-APC-glycogen synthase kinase-3β complex in the cytoplasm. After phosphorylation by glycogen synthase kinase-3β and CK1, β-catenin is degraded through the ubiquitin pathway. In the Wnt on-state, DVL inactivates the APC[2] complex for the degradation of β-catenin, and β-catenin is accumulated in the cytoplasm (3, 4). The stabilized β-catenin then translocates to the nucleus and associates with TCF/LEF transcription factors, which activate the Wnt target genes (5, 6). Thus, nuclear translocation of β-catenin is a key step in canonical Wnt signaling. In *Xenopus*, nuclear accumulation of β-catenin at the dorsal side is important for axis formation and expression of Wnt target genes during early embryogenesis (7). Overexpression of *Xwnt-8*, β-catenin, and *DVL2* induces a secondary axis and expression of Wnt target genes, such as Siamois, *Xnr3*, and *Xtwn*, at the ventral side (8–13).

IQGAP1 is a scaffolding protein and is highly conserved throughout the evolution from yeast to human (14). IQGAP1 is a 190-kDa and contains multiple protein-interacting domains; the CHD (calponin homology) domain binds to actin, the WW domain binds to ERK2, the IQ repeat motifs bind to calmodulin and myosin light chain, the RasGAP-like domain binds to Cdc42 and Rac1, and the RasGAP_c domain at the C terminus binds to β-catenin and E-cadherin (15–21). IQGAP1 is involved in various cellular processes including cytoskeletal reorganization, cell adhesion, and cell cycle (22). It is also reported that IQGAP1 stimulates β-catenin-mediated transcriptional activation (20). Despite the presence of the RasGAP-like domain, IQGAP1 demonstrates no GAP activity (23). However, IQGAP1 is known as a potential effector of Cdc42 and Rac (23). The subcellular localization of IQGAP1 occurs in a variety of cultured cells, and IQGAP1 is localized in the cytoplasm, cell membrane, and nucleus (24). These subcellular localizations are presumably linked to its cellular functions. Our recent study showed that IQGAP1 binds to DVL and translocates DVL into the nucleus in canonical Wnt signaling (25).

The importin-β family includes more than 20 genes and mediates the translocation of proteins that have the nuclear localizing signal (NLS) by making a complex with importin-α in the classical nuclear transport of proteins (26–28). Importin-β genes also mediate the translocation of non-NLS proteins by directly binding to them (29). The transport direction of importin-β-cargo complex is determined by the gradient of different nucleotide-bound states of a small GTPase, Ran. In the nucleus, the Ran guanine exchange factor RCC1 (RanGEF) converts the inactive form of Ran (RanGDP) to the active form (RanGTP). In the cytoplasm, most of the Ran is in the GDP-bound form because of the GTPase-activating protein RanGAP (27). At the nucleoplasmic side of the nuclear pore, RanGTP binds to importin-β, and a target protein is dissociated from the importin-β-cargo complex (27).

In the present study, we found that IQGAP1 complexed with DVL and β-catenin. Complex of these proteins mutually contributed to their nuclear localization. The depletion of endogenous IQGAP1 in *Xenopus* embryos suppressed secondary axis

* This work was supported by grants-in-aid for scientific research from the Ministry of Education, Science, Sports, and Culture of Japan.
[1] To whom correspondence should be addressed. Tel/Fax.:81-3-5803-4901; E-mail: shibuya.mcb@mri.tmd.ac.jp.
[2] The abbreviations used are: APC, adenomatosis polyposis coli; GAP, GTPase-activating protein; GEF, guanine nucleotide exchange factor; NLS, nuclear localizing signal; MO, morpholino oligonucleotide; xIpo-β5, *Xenopus* importin-β5; x, *Xenopus*; IQGAP1, IQ motif containing GTPase-activating protein 1; Importin-β5, karyoherin β family protein; DVL, Dishevelled.

induction and expression of Wnt target genes. We also found that IQGAP1 associated with importin-β5 and that the depletion of importin-β5 reduced the nuclear localization of β-catenin and expression of Wnt target genes. Moreover, it was suggested that Ran plays important roles in the canonical Wnt signaling pathway. These results reveal a novel role for IQGAP1 in modulating the subcellular localization and transcriptional activation of components of the Wnt signaling pathway.

EXPERIMENTAL PROCEDURES

Plasmid Construction—The *Xenopus xIpo-β5*, *xRan1*, *xRanGAP*, and *xRanGEF* were amplified by RT-PCR from cDNA templates prepared from *Xenopus* embryos and subcloned into the pCS2+ vectors. xIQGAP1-ΔRGD was constructed by PCR and contained the following amino acid sequences: xIQGAP1, 1–1013 and 1372–1657 amino acids. We made a GFP construct of β-catenin by conjugating it to the GFP sequence at the C terminus. The nuclear localization signal, PKKKRKV (30), is conjugated to the N terminus of β-catenin to construct the NLS-β-catenin. The active (GTP-bound) form of Ran proteins has double amino acid substitutions (G19V and Q69L). The inactive (GDP-bound) form of Ran proteins has single amino acid substitutions (T24N). Other constructs were previously reported (25).

Embryo Handling and Morpholino Oligonucleotides—Capped mRNAs were synthesized from linearized vectors using the mMESSAGE mMACHINE kit (Ambion). The morpholino oligonucleotides (MOs) (Gene Tools, LLC) used here were previously reported (25), and the sequences used were: 5′-TTTCAACCGTTTCCAAAGAACCAGG-3′ (β-catenin-MO), 5′-CCGCCATTGCTGCTGCTCCAGAAAC-3′ (*xIpo-β5*-MO), and 5′-AGTTTGTCAGCCTTCCAGAAGCGTC-3′ (*xRan1*-MO). The specificity of each MO was confirmed by its ability to inhibit the translation of FLAG-tagged mRNAs containing the targeted site with or without 5′-mismatched sequences. MO- (10 ng) and FLAG-tagged mRNAs (100 pg) were co-injected with β-globin-FLAG mRNA (100 pg) as loading control into the animal poles of four-cell stage embryos, and the injected animal caps were dissected at stage 10. Lysates from the animal caps were subjected to Western blotting with anti-FLAG antibody (M2, Sigma) (data not shown).

MOs and mRNAs were injected into four animal blastomeres at the eight-cell stage for dissection of animal caps or into two dorsal or ventral blastomeres at the four-cell-stage for quantitative RT-PCR analysis and observation of embryo phenotypes. Animal cap explants of the injected (10 pg of mRNA of each GFP-fused construct) embryos were dissected at the early gastrula stage (stage 10) and fixed for DAPI staining as reported previously (31). We counted the number of cells that have fluorescence signals as in our previous study (25). Dorsal or ventral sectors of the injected embryos were dissected at stage 10, and total RNA was extracted for RT-PCR analysis. The cytoplasmic and nuclear fractions were prepared as described with modifications (32).

RT-PCR Analysis—Total RNA was prepared using TRIzol (Invitrogen). cDNA synthesis was carried out using Moloney murine leukemia virus reverse transcriptase (Invitrogen). Quantitative PCR was performed with an Applied Biosystems 7300 real-time PCR cycler (ABI) using THUNDERBIRD SYBR quantitative PCR mix (TOYOBO). The sequences of the primer pairs were previously reported (25). *Xenopus* embryonic ornithine decarboxylase (*ODC*) was used for normalization of cDNA samples.

Chromatin Immunoprecipitation (ChIP) Assay—MYC-tagged mRNAs were injected into two dorsal blastomeres of four-cell embryos. Injected dorsal sectors were dissected at stage 10 and cross-linked in 1% formaldehyde for 1 h. Sonication, immunoprecipitation, and DNA purification were performed as described previously (33). The nested PCR was performed using specific primers as follows: Siamois: outer/forward, 5′-GAAGTCTTGCCAACTTCTCTCA-3′; outer/reverse, 5′-GTCCTTTGATGATTCTGATGAC-3′; inner/forward, 5′-CCAACTTCTCTCACTCAGTC-3′; and inner/reverse, 5′-TTTCCCTTGATCTTGCCC-3′; *Xnr3*: outer/forward, 5′-ATAGCTTTAATGTGCCACAATCTAC-3′; outer/reverse, 5′-GTACAGTCTTGGGAGTTCCCTG-3′; inner/forward, 5′-CATAAAGGCAAATGGTTTCTGC-3′; and inner/reverse, 5′-TTATACTGGGATGGACAGAGGC-3′.

Antibodies, Cell Lines, and siRNA Transfection—The following antibodies were used for immunoprecipitation and/or Western blotting analysis: horseradish peroxidase-conjugated anti-mouse IgG (GE Healthcare); horseradish peroxidase-conjugated anti-rabbit IgG (GE Healthcare); anti-FLAG (M2 and F7425, Sigma); anti-MYC (9B11, Cell Signaling); anti-DVL1 (3F12 and Q-25, Santa Cruz Biotechnology); anti-IQGAP1 (H-109, Santa Cruz Biotechnology); anti-β-catenin (C2206, Sigma); anti-importin-β5 (sc-11369, Santa Cruz Biotechnology); anti-Ran (sc-20802, Santa Cruz Biotechnology); anti-active-Ran (26915, NewEast Biosciences); anti-β-tubulin (sc-58884, Santa Cruz Biotechnology); and anti-histone-H3 (sc-10809, Santa Cruz Biotechnology). We used the following cell lines: HEK 293 cells, HEK 293T cells, SW480 cells, L cells, and L Wnt3A cells (25). Recombinant human Wnt3A (R&D Systems; 20 ng/ml) or 3 day *Wnt-3A* conditioned medium from L-Wnt-3A cells was used for Wnt stimulation of cultured cells. The FLAG peptide (F3290, Sigma; 100 μg/ml) was used for elution of FLAG tag proteins before the second immunoprecipitation. The growth medium for each cell type was as recommended by the American Type Culture Collection.

Protein Identification by LC-MS/MS Analysis—FLAG-human IQGAP1 was expressed in HEK 293 cells, and associated proteins were recovered from cell extracts by immunoprecipitation with anti-FLAG antibody. The IQGAP1-associated complexes were digested with *Achromobacter* protease I, and the resulting peptides were analyzed using a nanoscale LC-MS/MS system, as described previously (34).

GST Pulldown, GAP, and GEF Assay—GST-xRan1-FLAG was expressed in *Escherichia coli* BL21 (DE3). Bacteria were lysed with GST lysis buffer (PBS with 1% Triton X-100, 1 mM DTT, and Complete protease inhibitor cocktail (Roche Applied Science)). GST fusion proteins were purified by affinity chromatography with glutathione-Sepharose 4B (GE Healthcare) and eluted with 50 mM Tris-HCl (pH 8.0) and 20 mM glutathione. Purified proteins were mixed in TNE buffer (10 mM Tris-HCl (pH 7.8), 0.1% Nonidet P-40, 150 mM NaCl, 1 mM EDTA, 1 mM DTT, 10% glycerol, and Complete protease inhibitor cocktail (Roche Applied Science)). The protein solutions were

added to glutathione-Sepharose 4B (GE Healthcare) and incubated for 2 h at 4 °C. The GAP or GEF activity toward xRan1 was examined by the Western blotting of immunoprecipitates with the anti-active-Ran antibody. Each reaction performed in 50 μl of buffer A (50 mM HEPES, pH 7.4, 1.5 mM magnesium chloride, 5 mM EGTA, 1 mM DTT, 1 mM ATP, and Complete protease inhibitor cocktail (Roche Applied Science)) with the addition of 1 μl of cell lysate. Cell lysates were prepared from HEK 293T cells transfected with xIQGAP1-MYC, xRanGAP-MYC, xRanGEF-MYC, or pCS2+, using buffer B (buffer A + 150 mM sodium chloride, 10% glycerol, 1% Triton X-100, 60 mM magnesium chloride). Reactions were incubated at room temperature for 5 min and terminated by adding 250 μl of buffer B. We performed immunoprecipitation with the same tubes for 30 min. For GAP assays, GST-xRan1-FLAG was preloaded with GTP (1 mM) for 10 min at room temperature. For GEF assays, we added 0.1 mM GTP and 0.1 mM GDP in reactions.

RESULTS

IQGAP1 Forms a Complex with β-Catenin and DVL—In canonical Wnt signaling, the nuclear translocation of β-catenin is very important for transactivation of Wnt target genes (4). Our recent study has shown that xIQGAP1 plays a role in the translocation of xDVL2 into the nucleus in the canonical Wnt signaling pathway (25). Because both IQGAP1 and DVL bind to β-catenin (14, 25, 35), we examined whether IQGAP1 also contributes to the nuclear localization of β-catenin. The interaction of ectopically expressed *Xenopus* β-catenin with xDVL2 and xIQGAP1 was confirmed in HEK 293T cells (Fig. 1, *A* and *B*). The endogenous interaction of human β-catenin to both human DVL1 and human IQGAP1 was also confirmed in SW480 cells, which possess a mutation in the *APC* gene that interferes with β-catenin turnover (Fig. 1*C*). To investigate whether these proteins could form a complex, we performed a stepwise immunoprecipitation of β-catenin with xDVL2 and xIQGAP1. We detected an association of xDVL2 and β-catenin with xIQGAP1 in the first immunoprecipitation (Fig. 1*D*). In the second immunoprecipitation, we detected the binding of β-catenin to xDVL2 (Fig. 1*D*). The Wnt stimulation increased the binding of β-catenin in the second immunoprecipitates (Fig. 1, *D* and *E*). We also conducted this stepwise immunoprecipitation in a different order and obtained the same results; xIQGAP1 and β-catenin were found associated with xDVL2 in the first immunoprecipitation, and the β-catenin was associated with xIQGAP1 in the second immunoprecipitation (data not shown). These results suggest that xIQGAP1, xDVL2, and β-catenin can form a complex and that their association was increased by Wnt stimulation.

IQGAP1 Is Required for Nuclear Localization of β-Catenin—We then asked whether IQGAP1 and xDVL2 also contribute to the nuclear localization of β-catenin induced by Wnt signaling. We examined the distribution of β-catenin fused to GFP (β-catenin-GFP) in *Xenopus* embryonic (animal cap) cells injected with a morpholino oligonucleotide of *xIQGAP1*-MO or *xDVL2*-MO. We also examined the effect of depleting β-catenin on the nuclear localization of xDVL2-GFP and xIQGAP1-GFP. We detected nuclear localization of β-catenin when *Xwnt-8* was co-expressed in animal cap cells (Fig. 1*F*). Depletion of xIQGAP1 reduced the proportion of β-catenin-GFP localized in the nucleus in cells co-expressing *Xwnt-8* (Fig. 1, *F* and *G*, *lane 5*), whereas depletion of xDVL2 did not affect the nuclear localization of β-catenin (Fig. 1*G*, *lane 6*). We therefore examined whether the other xDVL family members, *i.e.* xDVL1 and xDVL3, may be involved in the nuclear localization of β-catenin. We found that depletion of all three xDVLs (xDVL1, xDVL2, and xDVL3) reduced the nuclear localization of β-catenin in cells co-expressing *Xwnt-8* (Fig. 1, *F* and *H*, *lanes 2* and *4*). We confirmed that depletion of xIQGAP1 or xDVLs reduced the amounts of β-catenin in the nuclear fractions of animal cap cells and did not alter the amounts of cytoplasmic β-catenin (Fig. 2, *upper panels*). Conversely, depletion of β-catenin by a morpholino oligonucleotide (β-catenin-MO) reduced the nuclear localization of both xDVL2-GFP and xIQGAP1-GFP in cells co-expressing *Xwnt-8* (Fig. 1, *I* and *J*, *lane 4*). Western blotting analysis also showed that the amounts of xDVL2 and xIQGAP1 in the nuclear fractions of animal cap cells were reduced by depletion of β-catenin (Fig. 2, *bottom panels*). To elucidate whether the interaction between xIQGAP1 and β-catenin is necessary for the nuclear localization of β-catenin, we made a C-terminal truncated construct of xIQGAP1, xIQGAP1-ΔC, which hardly bound to β-catenin (21) (Fig. 3*A*). Expression of xIQGAP1-ΔC reduced the nuclear localization of β-catenin-GFP in cells co-expressing *Xwnt-8* (Fig. 3*B*, *lane 4*) and did not rescue expression of Wnt target genes that were reduced by *xIQGAP1*-MO (Fig. 3*C*). These results indicate that Wnt-induced nuclear localization of β-catenin, xIQGAP1, and xDVL2 requires the mutual presence of all three components.

IQGAP1 Is Necessary for the Canonical Wnt Pathway—Our recent study showed that the depletion of endogenous IQGAP1 in *Xenopus* embryos suppressed secondary axis induction and expression of Wnt target genes (25). We confirmed that the induction of the Wnt target genes and partial secondary axis induced by β-catenin was suppressed by the depletion of xIQGAP1 (Fig. 3, *D* and *E*, *lane 2*). On the other hand, depletion of xIQGAP1 did not affect both of the Wnt target genes and the secondary axis formation induced by NLS-β-catenin, fusing with a peptide encoding NLS at the N terminus, which is predominantly localized in the nucleus without Wnt signaling stimulation (Fig. 3, *D* and *E*, lane4). Moreover, we examined whether xIQGAP1 affects the localization of NLS-β-catenin. We observed that the nuclear localization of NLS-β-catenin-GFP was not suppressed by *xIQGAP1*-MO or *xDVLs*-MO, (Fig. 3, *F* and *G*). To confirm whether xIQGAP1 affects the stabilization of β-catenin in cytoplasm, we investigated the amounts of cytoplasmic β-catenin. We observed that *xIQGAP1*-MO injection had no effect on the β-catenin stability in the cytoplasm of the dorsal marginal cells (Fig. 3*H*). Interestingly, the ChIP assay revealed that xIQGAP1 was not recruited to the promoter regions of the Wnt target genes, whereas both xDVL2 and β-catenin were recruited (Fig. 3*I*). These results suggest that xIQGAP1 functions as an intermediate molecule in the canonical Wnt signaling pathway in early development, promoting the nuclear localization of β-catenin.

Importin-β5 Regulates the Nuclear Localization of IQGAP1—To elucidate the mechanisms by which IQGAP1 is translocated

into the nucleus, we performed a high throughput analysis of proteins that co-immunoprecipitated with human IQGAP1 in HEK 293 cells. We identified human importin-β5 as a candidate protein that may interact with IQGAP1. Importin-β family proteins mediate the nuclear import of several proteins that bind directly to them (36). An interaction between ectopically expressed xIQGAP1 and ximportin-β5 (xIpo-β5) was confirmed in HEK 293T cells, but xDVL2 and β-catenin did not associate with xIpo-β5 (Fig. 4*A*). We also confirmed endogenous interaction between human IQGAP1 and human impor-

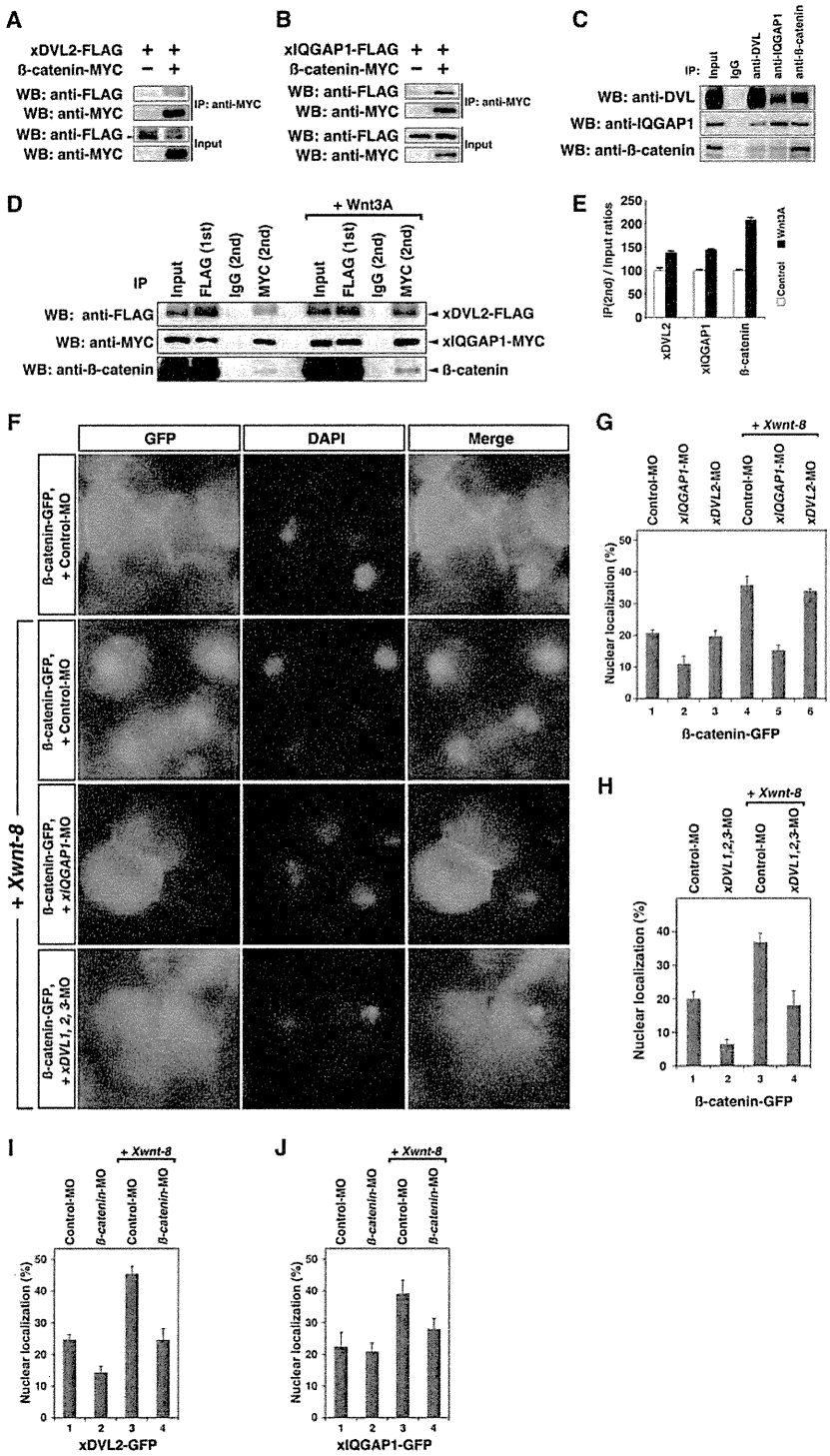

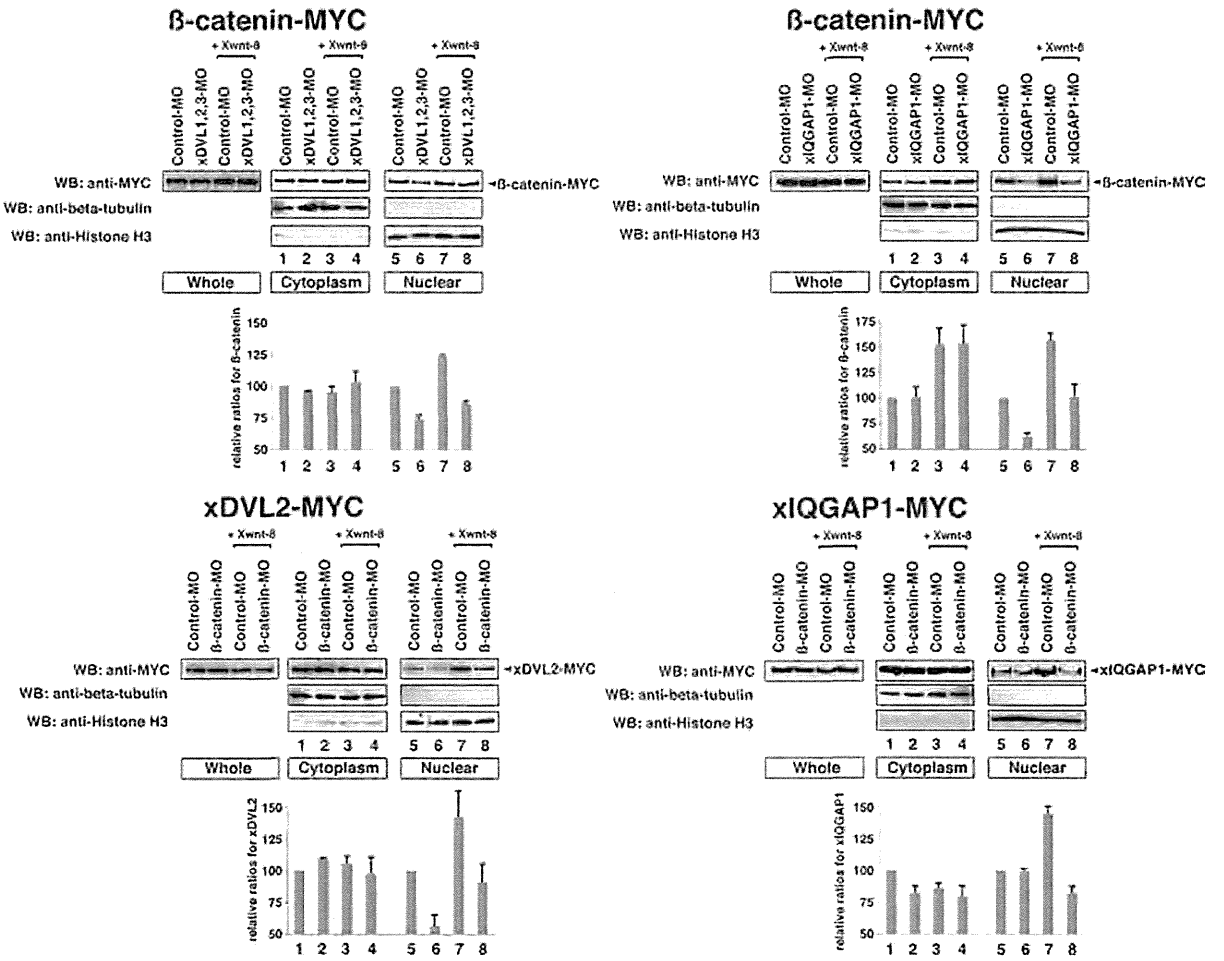

FIGURE 2. **Cytoplasmic and nuclear distribution of xDVL2, xIQGAP1, and β-catenin in animal cap cells.** Each MYC-tagged mRNA (100 pg) was co-injected into the animal poles of four-cell stage embryos with the indicated morpholino oligonucleotides, and the injected animal caps were dissected at stage 10. Lysates from the animal caps were fractionated and subjected to Western blotting (*WB*) with the indicated antibodies. *Upper panels*, β-catenin-MYC. *Lower panels*, *left*, xDVL2-MYC. *Lower panels*, *right*, xIQGAP1-MYC. In the case of β-catenin-MYC, cytoplasmic fraction was refractionated to cytosolic and membrane fractions.

tin-β5 in HEK 293T cells (Fig. 4*B*). The Wnt stimulation and the co-expression of xDVL2 and β-catenin increased the interaction between xIpo-β5 and xIQGAP1 (Fig. 4, *C* and *D*). Dorsal injection of *xIpo-β5*-MO reduced the endogenous expression of Wnt signal target genes (Fig. 4*E*). Expression of the Wnt target genes induced ectopically by *Xwnt-8* was also reduced by *xIpo-β5*-MO and induced by *xIpo-β5* (Fig. 4*F*). Depletion of xIpo-β5 reduced the nuclear localization of xIQGAP1-, xDVL2-, and β-catenin-GFP fusion proteins by co-expressing *Xwnt-8* in *Xenopus* animal cap cells (Fig. 4, *G–I*). On the other hand, overexpression of xIpo-β5 mRNA increased the nuclear localization of β-catenin-GFP nuclear localization (Fig. 4*J*). These results suggest that the interaction between xIQGAP1 and xIpo-β5 mediates the nuclear import of the xDVL2-xIQGAP1-β-catenin complex in Wnt signaling pathway.

Ran1 Plays a Role of Nuclear Localization of IQGAP1 in Canonical Wnt Signaling—The transport cycle of importin-β is regulated by a small GTPase, Ran (27, 37). To confirm whether

FIGURE 1. **Interaction between β-catenin, xDVL2, and xIQGAP1.** *A*, interaction between ectopically expressed xDVL2 and β-catenin in HEK 293T cells. *WB*, Western blotting; *IP*, immunoprecipitation. *B*, interaction between ectopically expressed xIQGAP1 and β-catenin in HEK 293T cells. *C*, interaction among endogenous β-catenin, hDVL1, and hIQGAP1 in SW480 cells. *D*, interaction among ectopically expressed β-catenin, xDVL2, and xIQGAP1 in HEK 293T cells. Anti-FLAG antibody was used for the first immunoprecipitation, and the precipitate was subjected to a second immunoprecipitation with IgG or MYC antibodies. *E*, the second immunoprecipitation/input ratios for xDVL2, xIQGAP1, and β-catenin in *panel D*. *F*, nuclear localization of β-catenin-GFP in stage 10 *Xenopus* animal cap cells overexpressing *Xwnt-8*. Control-MO (15 ng), *xIQGAP1*-MO (15 ng), or *xDVL1*-MO, *xDVL2*-MO, and *xDVL3*-MO (each 5 ng) was co-injected with β-catenin-GFP mRNA (10 pg). *Left*, GFP signals. *Center*, DAPI staining of animal cap cells. *Right*, merge. *G–J*, the ratio of cells that had nuclear fluorescence signals of GFP. The average of ratio was taken with six explants in three independent experiments. *Error bars* represent S.D. with six explants. *G*, the ratio of nucleus-localized β-catenin-GFP in cells injected with *xIQGAP1*-MO and *xDVL2*-MO. *Lane 1*, $n = 1770$, 20.6%; *lane 2*, $n = 1437$, 10.9%; *lane 3*, $n = 1662$, 19.6%; *lane 4*, $n = 1655$, 35.8%; *lane 5*, $n = 1763$, 15.2%; *lane 6*, $n = 1874$, 33.9%. *H*, the ratio of nucleus-localized β-catenin-GFP in cells injected with *xDVL1*-MO, *xDVL2*-MO, and *xDVL3*-MO. *Lane 1*, $n = 1858$, 19.9%; *lane 2*, $n = 4689$, 6.4%; *lane 3*, $n = 5382$, 36.8%; *lane 4*, $n = 3650$, 18.0%. *I*, the ratio of nucleus-localized xDVL2-GFP in cells injected with β-catenin-MO. *Lane 1*, $n = 971$, 24.6%; *lane 2*, $n = 989$, 14.2%; *lane 3*, $n = 347$, 45.5%; *lane 4*, $n = 326$, 24.5%. *J*, the ratio of nucleus-localized xIQGAP1-GFP in cells injected with β-catenin-MO. *Lane 1*, $n = 784$, 21.9%; *lane 2*, $n = 616$, 20.9%; *lane 3*, $n = 544$, 39.0%; *lane 4*, $n = 885$, 27.9%.

Ran is related to the nuclear import of IQGAP1 in the canonical Wnt signaling pathway, we investigated the effects of Ran in cultured cells and *Xenopus* embryos. We confirmed that both ectopically expressed xIQGAP1 and ectopically expressed xIpo-β5 bound to xRan1 (Fig. 5, *A* and *B*). The endogenous interaction of human Ran to both human IQGAP1 and human importin-β5 was also confirmed (Fig. 5, *C* and *D*). Dorsal injection of *xRan1*-MO reduced the endogenous expression of Wnt signal target genes at the gastrula stage (Fig. 5*E*). We also found that the expression of the Wnt target genes induced by ventral injection of *Xwnt-8* was reduced by depletion of xRAN1 and that its reduction was rescued by *xRan1* mRNA (Fig. 5*F*). The injection of both *xIpo-β5*-Mo and *xRan1*-MO synergistically reduced Wnt target gene expression induced by ventral injec-

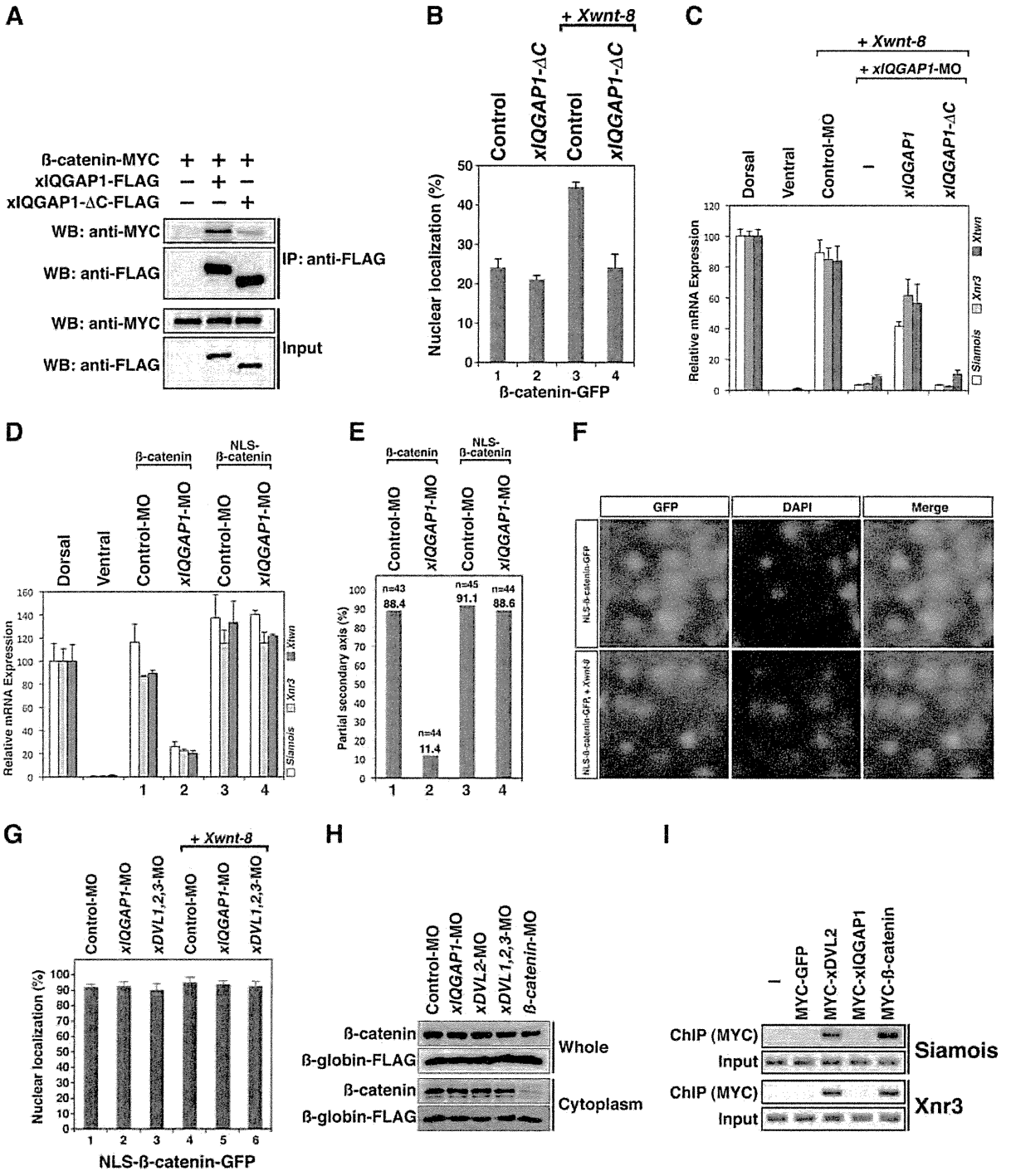

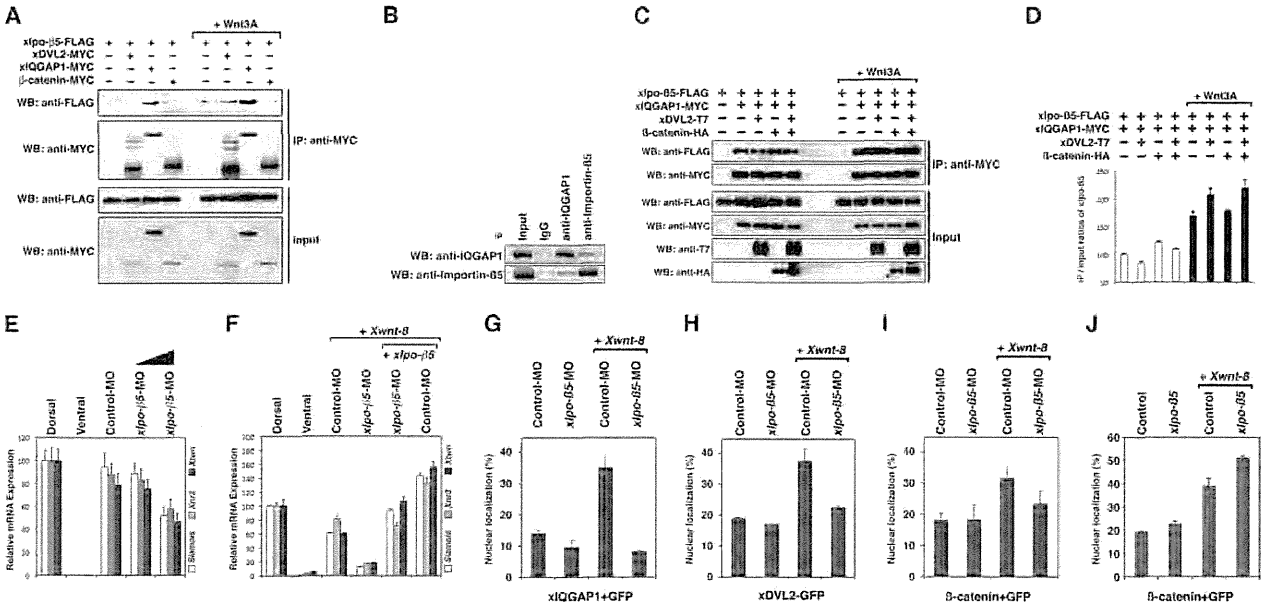

FIGURE 4. **Interaction between xIQGAP1 and xIpo-β5 in canonical Wnt signaling.** *A*, interaction between ectopically expressed xIpo-β5 and xDVL2, xIQGAP1, and β-catenin in HEK 293T cells. *WB*, Western blotting; *IP*, immunoprecipitation. *B*, interaction between endogenous human IQGAP1 and human importin-β5 in HEK 293T cells. *C*, interaction between xIQGAP1 and xIpo-β5 with ectopically expressed xDVL2 and β-catenin in HEK 293T cells. Immunoprecipitates obtained using anti-MYC antibody were subjected to Western blotting with the indicated antibodies. +, present; −, absent. *D*, the immunoprecipitation/input ratios for xIpo-β5 in *panel C*. *Error bars* represent S.D. in three experiments. *E*, quantitative RT-PCR analysis of early dorsal Wnt target genes ($n = 3$). Control-MO (80 ng) or *xIpo-β5*-MO (low dose: 40 ng, high dose: 80 ng) was injected into two dorsal blastomeres of four-cell embryos. The following procedure was described in Fig. 3C. *F*, quantitative RT-PCR analysis of early dorsal Wnt target genes ($n = 3$). Control-MO (40 ng), *xIpo-β5*-MO (40 ng), and *Xwnt-8* (0.5 pg) mRNA were ventrally co-injected with *xIpo-β5* mRNA (500 pg). *G–J*, the ratio of GFP-fused constructs localized in the nucleus in cells injected with *xIpo-β5*-MO or *xIpo-β5* mRNA. *G*, xIQGAP1-GFP. *Lane 1*, $n = 1859$, 14.0%; *lane 2*, $n = 1216$, 9.7%; *lane 3*, $n = 909$, 35.1%; *lane 4*, $n = 887$, 8.3%. *H*, xDVL2-GFP. *Lane 1*, $n = 932$, 18.9%; *lane 2*, $n = 540$, 16.9%; *lane 3*, $n = 669$, 37.2%; *lane 4*, $n = 402$, 22.4%. *I*, β-catenin-GFP. *Lane 1*, $n = 1125$, 18.3%; *lane 2*, $n = 636$, 18.5%; *lane 3*, $n = 1317$, 40.0%; *lane 4*, $n = 752$, 23.7%. *J*, β-catenin-GFP. *Lane 1*, $n = 495$, 19.4%; *lane 2*, $n = 966$, 22.8%; *lane 3*, $n = 796$, 39.2%; *lane 4*, $n = 399$, 51.4%. *Error bars* represent S.D. with six explants.

tion of *Xwnt-8* (Fig. 5*G*). In addition, depletion of xRan1 reduced the nuclear localization of β-catenin-GFP by co-expressing *Xwnt-8* in animal cap cells (Fig. 5*H*). On the other hand, overexpression of xRan1 mRNA increased the nuclear localization of β-catenin-GFP nuclear localization (Fig. 5*I*). We confirmed that both depletions of xIpo-β5 and xRan1 did not affect the stability of cytoplasmic β-catenin (Fig. 5*J*). Interestingly, the Ras-GAP domain-deleted xIQGAP1 construct, xIQGAP1-ΔRGD, did not bind to xRan1 (Fig. 6*A*) and xIpo-β5 (Fig. 6*B*). The expression of *xIQGAP1-ΔRGD* did not rescue expression of Wnt target genes that were reduced by *xIQGAP1*-MO (Fig. 6*C*) and reduced the nuclear localization of β-catenin-GFP in the Xwnt-8-expressing cells (Fig. 6*D*). These results suggest that the interaction between xIQGAP1 and xIpo-β5, or xIQGAP1 and xRan1, is indispensable for the function of xIQGAP1 in Wnt signaling. Interestingly, the expression of xIQGAP1 in HEK 293T cells increased the GTP-bound activated form of xRan1 in the same way as the effect of xRanGEF (Fig. 6*E*), but the interaction between xIQGAP1 and either xRanGAP or xRanGEF was not observed (Fig. 6*F*). The hydrolysis of xRAN1 by xRanGAP was reduced by xIQGAP1 (Fig. 6*G*), and the expression of xIQGAP1 inhibited the interaction between the active form of xRAN1 and xRanGAP (Fig. 6*H*). These results suggest that xIQGAP1 has no GAP activity but

FIGURE 3. **The role of xIQGAP1 in canonical Wnt signaling.** *A*, interaction between ectopically expressed β-catenin and xIQGAP1 or xIQGAP1-ΔC in HEK 293T cells. *B*, the ratio of β-catenin-GFP localized in the nucleus in cells injected with *xIQGAP1-ΔC* mRNA. *Lane 1*, $n = 635$, 24.3%; *lane 2*, $n = 1517$, 21.2%; *lane 3*, $n = 459$, 44.7%; *lane 4*, $n = 1271$, 24.3%. *C*, quantitative RT-PCR analysis of early dorsal Wnt target genes ($n = 3$). Control-MO (15 ng) or *xIQGAP1*-MO (15 ng) was co-injected with *xIQGAP1* (400 pg) or *xIQGAP1-ΔC* (400 pg) mRNA into two ventral blastomeres of four-cell embryos. RNAs from dissected ventral sectors of injected embryos were extracted at stage 10. RNAs from dissected dorsal and ventral sectors of uninjected embryos were used as controls. The value obtained for each gene was normalized to the level of *ODC* (ornithine decarboxylase). The value of dorsal sectors was set to 100, and other values were computed. *Error bars* represent S.D. in three experiments. *D*, quantitative RT-PCR analysis of early dorsal Wnt target genes ($n = 3$). Control-MO (15 ng) or *xIQGAP1*-MO (15 ng) was co-injected with β-catenin (20 pg) or NLS-β-catenin (20 pg) mRNA into two ventral blastomeres of four-cell embryos. The following procedure is indicated in *panel C*. *E*, the ratio of injected embryos exhibiting a partial secondary axis. The *numbered lanes* indicate the injected mRNAs and MOs consistent with the numbering in *panel D*. *F*, nuclear localization of NLS-β-catenin-GFP in stage 10 *Xenopus* animal cap cells overexpressing *Xwnt-8*. *Left panels*, GFP signals. *Center panels*, DAPI staining. *Right panels*, merge. *G*, the ratio of nucleus-localized NLS-β-catenin-GFP in cells injected with *xIQGAP1*-MO and *xDVL1-, 2-, 3*-MO in *Xenopus* animal cap cells at stage 10. *Lane 1*, $n = 352$, 92.0%; *lane 2*, $n = 347$, 92.5%; *lane 3*, $n = 396$, 89.9%; *lane 4*, $n = 907$, 94.7%; *lane 5*, $n = 512$, 93.6%; *lane 6*, $n = 359$, 92.4%. *H*, Western blotting analysis using β-catenin antibody. Control-MO (15 ng), *xIQGAP1*-MO (15 ng), *xDVL2*-MO (15 ng), *xDVLs*-MO (*xDVL1*-MO (5 ng), *xDVL2*-MO (5 ng), *xDVL3*-MO (5 ng), or β-catenin-MO (15 ng) was co-injected with β-globin-FLAG mRNA (100 pg) into two dorsal blastomeres of four-cell embryos. Lysates from whole embryos or cytoplasmic fractions were obtained dissected dorsal sectors at stage 10 and were subjected to Western blotting with the β-catenin and FLAG antibodies. *I*, ChIP assay for Siamois and *Xnr3* promoter regions. Each indicated mRNA (200 pg) was injected into two dorsal blastomeres of four-cell embryos. Injected dorsal sectors were dissected and cross-linked at stage 10. Immunoprecipitates using anti-MYC antibody were examined by PCR using specific primers of Siamois and *Xnr3* promoter regions.